

The LaGrange Tornado during VORTEX2. Part I: Photogrammetric Analysis of the Tornado Combined with Single-Doppler Radar Data

ROGER M. WAKIMOTO

National Center for Atmospheric Research, Boulder, Colorado*

NOLAN T. ATKINS

Department of Atmospheric Sciences, Lyndon State College, Lyndonville, Vermont

JOSHUA WURMAN

Center for Severe Weather Research, Boulder, Colorado

(Manuscript received 8 July 2010, in final form 14 November 2010)

ABSTRACT

This study presents a single-Doppler radar analysis combined with cloud photography of the LaGrange, Wyoming, tornado on 5 June 2009 in an attempt to relate the radar-observed hook echo, weak-echo hole (WEH), and rotational couplet to the visual characteristics of the tornado. The tornado was rated EF2. The circulation at low levels went through two intensification periods based on azimuthal shear measurements. The first intensification was followed by the appearance of a brief funnel cloud. The second intensification was coincident with the appearance of a second funnel cloud that remained in contact with the ground until the tornado dissipated.

A deep WEH rapidly formed within the hook echo after damaging wind was identified at the ground and before the appearance of a funnel cloud. The echo pattern through the hook echo on 5 June undergoes a dramatic evolution. Initially, the minimum radar reflectivities are near the surface (<15 dBZ) and the WEH does not suggest a tapered structure near the ground. Subsequently, higher reflectivities appear at low levels when the funnel cloud makes contact with the ground. During one analysis time, the increase of the echo within the WEH at low levels results in a couplet of high/low radar reflectivity in the vertical. This increase in echo at low levels is believed to be associated with lofted debris although none was visibly apparent until the last analysis time. The WEH was nominally wider than the visible funnel cloud. The dataset provides the first detailed analysis of the double-ring structure within a hook echo that has been reported in several studies. The inner high-reflectivity region is believed to be a result of lofted debris. At higher-elevation angles, a small secondary WEH formed within the first WEH when debris was lofted and centrifuged.

A feature noted in past studies showing high-resolution vertical cross sections of single-Doppler velocity normal to the radar beam is an intense rotational couplet of negative and positive values in the lowest few hundred meters. This couplet was also evident in the analysis of the LaGrange tornado. The couplet was asymmetric with stronger negative velocities owing to the motion of the tornado toward the radar. The damaging wind observed by radar extended well beyond the condensation funnel in the lowest few hundred meters. However, another couplet indicating strong rotation was also noted aloft in a number of volume scans. The decrease in rotational velocities between the low- and upper-level couplets may be related to air being forced radially outward from the tornado center at a location above the intense inflow.

* The National Center for Atmospheric Research is sponsored by the National Science Foundation.

Corresponding author address: Roger M. Wakimoto, NCAR, P.O. Box 3000, Boulder, CO 80307.
E-mail: wakimoto@ucar.edu

1. Introduction

A major milestone was reached in the operational detection of severe weather when the hook echo was first observed by radar and shown to be associated with tornadogenesis (Stout and Huff 1953; Forbes 1981). Subsequent studies examining radial velocities based on

Doppler radars measurements were able to resolve the mesocyclone and the tornadic-vortex signature (TVS), which can be associated with the parent circulation of the tornado and the tornado, respectively (e.g., Brown et al. 1978). More recently, successful intercepts of supercell storms with mobile Doppler radars have provided unprecedented, close-up views of the structure of the hook echo and the intense circulation within and surrounding the tornado (e.g., Bluestein et al. 1993, 1997, 2004, 2007a,b; Wurman et al. 1996a; Wurman and Gill 2000; Alexander and Wurman 2005; Wurman et al. 2007a,b). One of the characteristic features within the hook echo is the weak-echo hole (WEH), first documented by Fujita (1981). The WEH appears inside the tornado core and is surrounded by a high-reflectivity tube that is wider than the tornado (e.g., Fujita 1981; Wurman et al. 1996a; Wakimoto et al. 1996; Wurman and Gill 2000; Bluestein et al. 2004, 2007b) and is likely caused by the centrifuging of hydrometeors and debris (Dowell et al. 2005).

While these past studies have collected a plethora of data on the echo structure and velocity fields in tornadoes, careful analysis of pictures taken at the same time have been relatively rare (Bluestein et al. 1993, 1997, 2004, 2007a,b; Wakimoto et al. 2003). Photogrammetric analysis is important since it provides quantitative information about the tornado (e.g., condensation funnel width). The X-, C-, or S-band radars do not detect signals in regions characterized by small cloud drops. In addition, few studies have attempted to merge Doppler radar data with tornado photographs. Wakimoto et al. (2003), Dowell et al. (2005), and Rasmussen and Straka (2007) superimposed interpolated radar reflectivity and Doppler velocity data onto a picture of the tornado but only for a single time. Wakimoto and Martner (1992) provided a photogrammetric and Doppler radar analysis of the entire life cycle of a Colorado tornado, however, it was associated with a nonsupercell storm (i.e., the tornado was not associated with a mesocyclone).

This paper presents an analysis of a tornado that developed west of LaGrange, Wyoming, on 5 June 2009 during the Verification of the Origins of Rotation in Tornadoes Experiment II (VORTEX2). VORTEX2 was a large multiagency field project that operated 10 May–13 June 2009 and focused on collecting high-resolution data on tornadoes and tornadic storms (Wurman et al. 2010). The experiment was atypical in that the fleet of instrumentation was mobile during the entire field phase. Facilities included 10 mobile radars, mobile mesonet instrumented vehicles, weather balloon launching vans, photography teams, and other instruments. Many of the vehicles traveled over 16 000 km across the southern and central plains while intercepting a number of supercell

storms during 2009. The primary radar dataset used in this study was collected by the Doppler-on-Wheels (DOW; Wurman et al. 1997; Wurman 2001).

The LaGrange tornado was scanned by several radars while the evolution of the funnel was captured by a series of photographs and high-definition video. In this paper, single-Doppler radar data are combined with these photographs in an attempt to relate the hook echo, WEH, and rotational couplet to the visual characteristics of the tornado. The DOW radars and the cloud photogrammetry technique are discussed in section 2. Section 3 presents a brief discussion of the environmental conditions, an overview of the data collected on the storm, the hook echo, and the tornado. The azimuthal shear associated with the tornado at low levels is shown in section 4 and detailed vertical cross sections of radar reflectivity and single-Doppler velocities merged with pictures of the tornado are discussed in section 5. A summary and conclusions are presented in section 6.

2. DOW radars and cloud photogrammetry

The DOWs (data from the DOW6 and DOW7 radars are used in this study) are 3-cm mobile Doppler radars mounted on trucks and have been used extensively to collect data near severe local storms (e.g., Wurman and Gill 2000). During the deployment near the LaGrange tornado, the DOWs scanned at 50° s^{-1} , employed 250-ns pulses at 4000-Hz pulse repetition frequency, and sampled returned signals to retrieve 60-m gate spacing. The peak transmitted power is 250 kW. The 2.44-m parabolic antennas produce beam widths of 0.93° , typically oversampled every 0.3° during a horizontal scan. The radars executed coordinated volume scans every 2 min. It should be noted that analysis times were restricted to ~ 30 s at low levels within the 2-min volume scan. This reduced problems associated with time–space conversion. The emphasis in this paper is the series of elevation scans that were confined to low levels (i.e., 0.5° , 1° , 2° , 3° , 4° , 5° , and 6°). For more information about the DOWs, the interested reader is referred to Wurman et al. (1997) and Wurman (2001).

Photogrammetric analysis is a technique that can extract quantitative information from a picture such as the dimensions of a cloud or the condensation funnel accompanying a tornado (e.g., Malkus 1952; Rasmussen et al. 2003; Zehnder et al. 2007). Photogrammetry requires knowledge of the camera location and precise azimuth angles to targets located on the horizon in the picture. Spherical trigonometry can then be used to calculate the effective focal length and the tilt angle of the camera lens. Once these variables are known, a complete azimuth- and elevation-angle grid can be

constructed and superimposed on the photograph. An examination of the calculated azimuth-angle grid with known targets on the photograph suggests that errors range between 0.1° and 0.2° . A general discussion of photogrammetry can be found in Abrams (1952) and Holle (1986). Additional discussion of the process used to analyze the photos shown in this paper is presented in the appendix.

The photographs shown in this paper were taken from the same location as the DOW radars. Accordingly, the azimuth- and elevation-angle grid superimposed onto the photographs also represents the radar scanning angles. Subsequently, it is possible to select individual radar reflectivity and Doppler velocity data points (range gates) for the volume scan encompassing the time of the photograph and plot them on the picture. Section 4 will present vertical cross sections that were chosen to slice through the WEH and the rotational couplet. These analyses provide the highest possible resolution since the raw rather than interpolated radar data is used.

3. Environmental conditions, data collection, and the hook echo

The morning weather briefing on 5 June suggested possible targets in Colorado and in the eventually chosen region of the Nebraska Panhandle and southeast Wyoming where the low-level shear combined with mid and upper-level winds appeared to favor the development of tornadic supercells. The convective available potential energy (CAPE) was predicted to be $>1500 \text{ J kg}^{-1}$ throughout the area. Convective cells began developing in the early afternoon north northwest of Cheyenne, Wyoming. By ~ 2100 UTC, a right-moving supercell developed north of Cheyenne and was chosen as the storm that the mobile armada of instruments would intercept.

Figure 1 shows the initial deployment of DOW6 and DOW7 along an approximate north-south-oriented highway in Wyoming in order to collect dual-Doppler data. The radars were separated by ~ 15 km. Still photographs were taken at the same location as the radars as schematically illustrated in the figure. The hook echo, as outlined by the 45-dBZ isopleth, at 4 times based on low-level scans by the DOWs is plotted in the figure. A more complete presentation of the evolution of the hook echo from 2156:08 to 2216:07 UTC is shown in Fig. 2. A WEH is apparent in most of the low-level scans. The center of the rotational couplet that is evident in Fig. 2 was plotted in Fig. 1 and reveals the nonlinear path that the circulation followed until it dissipated soon after crossing Highway 85. The motion of the couplet was from $\sim 280^\circ$ at speeds that ranged between 9.1 and 9.6 m s^{-1} . Accordingly, the

azimuths labeled on photos A, B, and C in Fig. 1 reveal that the tornado was heading toward DOW7.

The surrounding terrain was hilly and relatively barren. As a result, the tornado did not cause significant damage based on a poststorm survey. A ground survey on 6 June followed by an aerial survey on 8 June, however, revealed a few downed trees, broken branches, and snapped telephone poles as shown in Fig. 1. The documented damage, radial velocities recorded by the DOWs, and in situ measurements by the Tornado Intercept Vehicle (TIV; Wurman et al. 2007c) resulted in EF2 rating for this tornado by the National Weather Service. The ground survey identified tornadic damage at ~ 2152 UTC (Fig. 1) near the location of the rotational couplet well before the appearance of a funnel cloud and WEH (to be shown later). The operators of the DOW7 radar, independently, reported tornadogenesis at 2152 UTC based on their real-time estimate of the strength of the couplet compared with numerous past intercepts of tornadic storms (i.e., a 40 m s^{-1} Doppler velocity difference across a circulation that is less than 2 km in diameter). The location of the tornado at the time of the four photographs (see Fig. 1) is shown by letter identifiers along the track.

4. Azimuthal shear

An examination of the azimuthal shear accompanying the rotational couplet during 2156–2217 UTC at low levels (0.5°) is presented in Fig. 3. There may be differences noted between the velocity images shown in Fig. 2 and the analysis presented in Fig. 3 due to the different elevation angles used. The size of the couplet is estimated based on the distance separating the strongest inbound and outbound radial velocities within the couplet (ΔX) and is plotted in the figure. The azimuthal resolution was increasing during this time period since the tornado was approaching DOW7. The dimension of the radar beamwidth is plotted in Fig. 3 to help quantify how the changes in resolution might impact the shear calculations.

There are two periods of increased azimuthal shear and contraction of the rotational couplet shown in Fig. 3. This behavior is qualitatively consistent with the conservation of angular momentum as noted by Bluestein et al. (2003) and in dual-Doppler studies (Wurman et al. 2007a). The first intensification started at ~ 2159 UTC and reached a peak at ~ 2201 UTC. A narrow funnel cloud formed around 2202:12 UTC and was visible for ~ 30 s (Fig. 3) while the shear was decreasing in strength. (Note: the decrease in azimuthal shear was largely a result of the increase in ΔX .) The changes of azimuthal shear at 1° were also examined (not shown) and were consistent with the findings shown in Fig. 3. As will be shown later, the data collected at 1° sliced through the

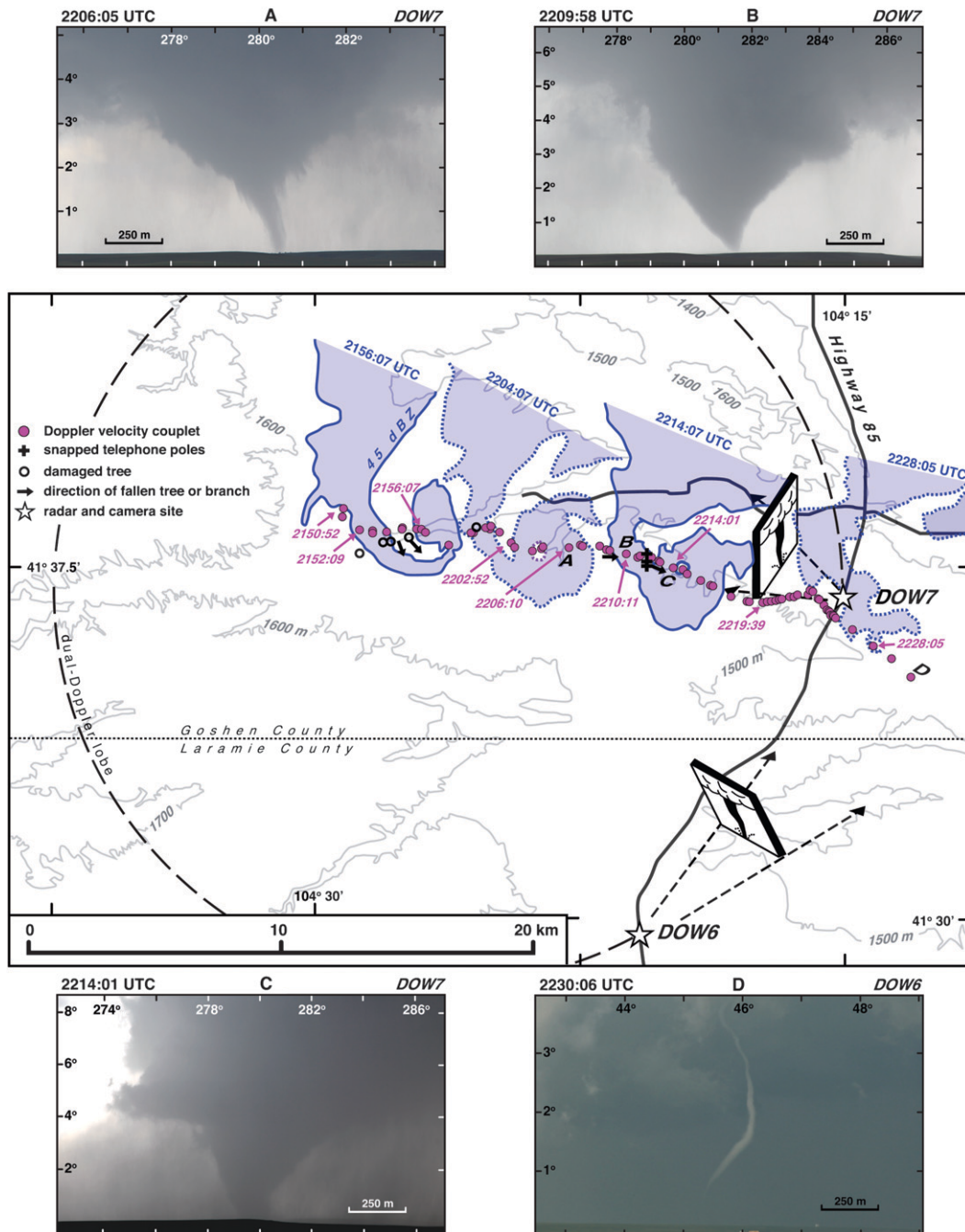


FIG. 1. Hook echo (1° elevation angle) associated with the LaGrange supercell storm at 2156:07, 2204:07, 2214:07, and 2228:05 UTC recorded from the DOW. Magenta dots represent the location of the tornadic rotational couplet based on low-level scans. Camera sites were collocated with the radars as schematically shown in the figure. Damage to telephone poles and trees are plotted (explanation of the symbols are shown in the legend). Photographs of the tornado at four locations along the track are shown (letter identifiers are plotted along the track). Photos A, B, and C were taken from the DOW7 location while D was taken from the DOW6 site. Photos were photogrammetrically enlarged or reduced so that the relative dimensions of the tornado can be estimated. The locations of DOW6 and DOW7 are shown by the stars. The primary dual-Doppler lobe is plotted.

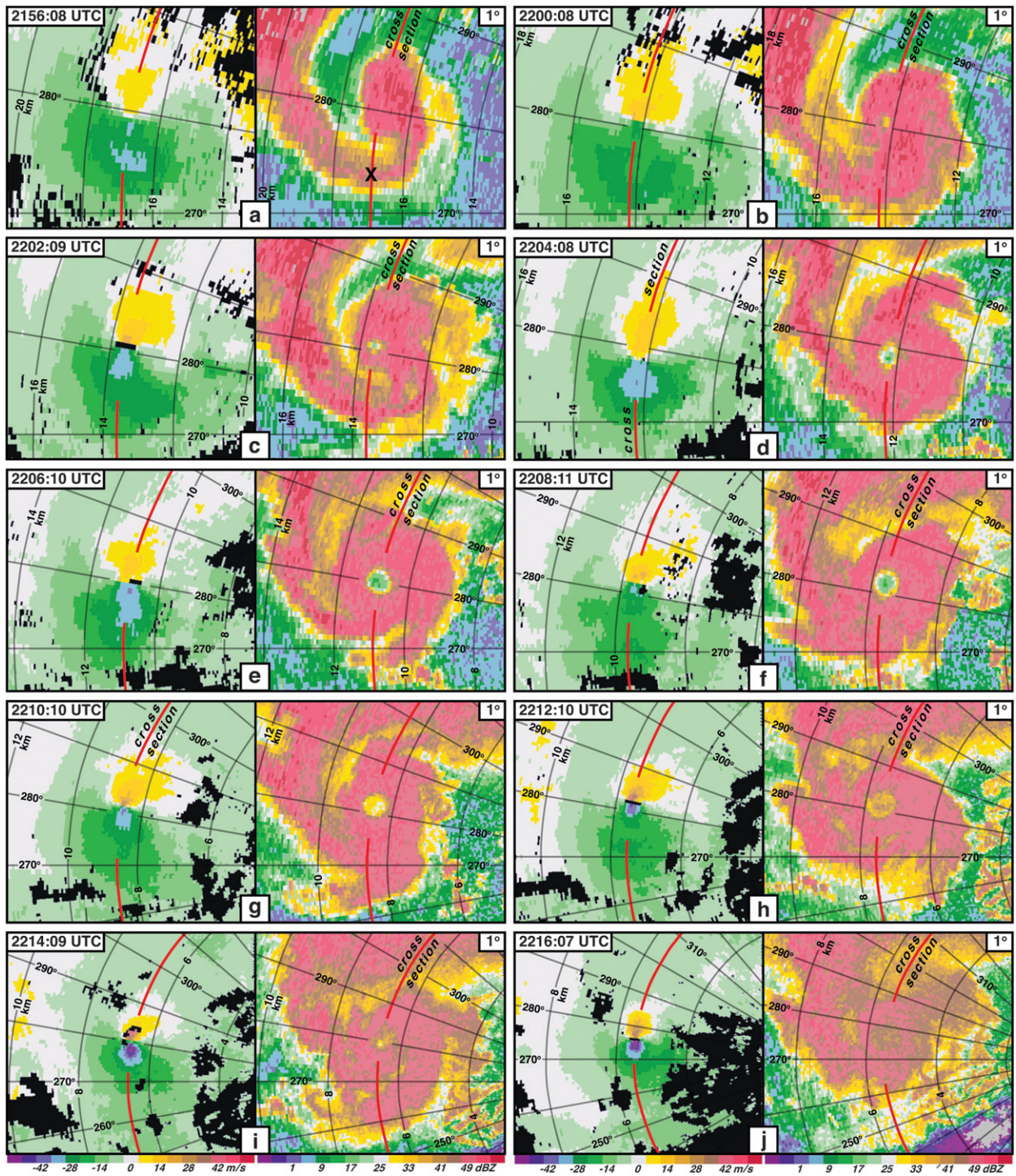


FIG. 2. A series of radar reflectivity and single-Doppler base velocities scans at 1° elevation angle from DOW7 at (a) 2156:08, (b) 2200:08, (c) 2202:09, (d) 2204:08, (e) 2206:10, (f) 2208:11, (g) 2210:10, (h) 2212:10, (i) 2214:09, and (j) 2216:07 UTC. Gray lines denote the range and azimuth angle grid. The red range ring denotes the location of vertical cross sections shown in Figs. 4–19. The letter “X” plotted on the reflectivity scan in (a) is shown in Fig. 4.

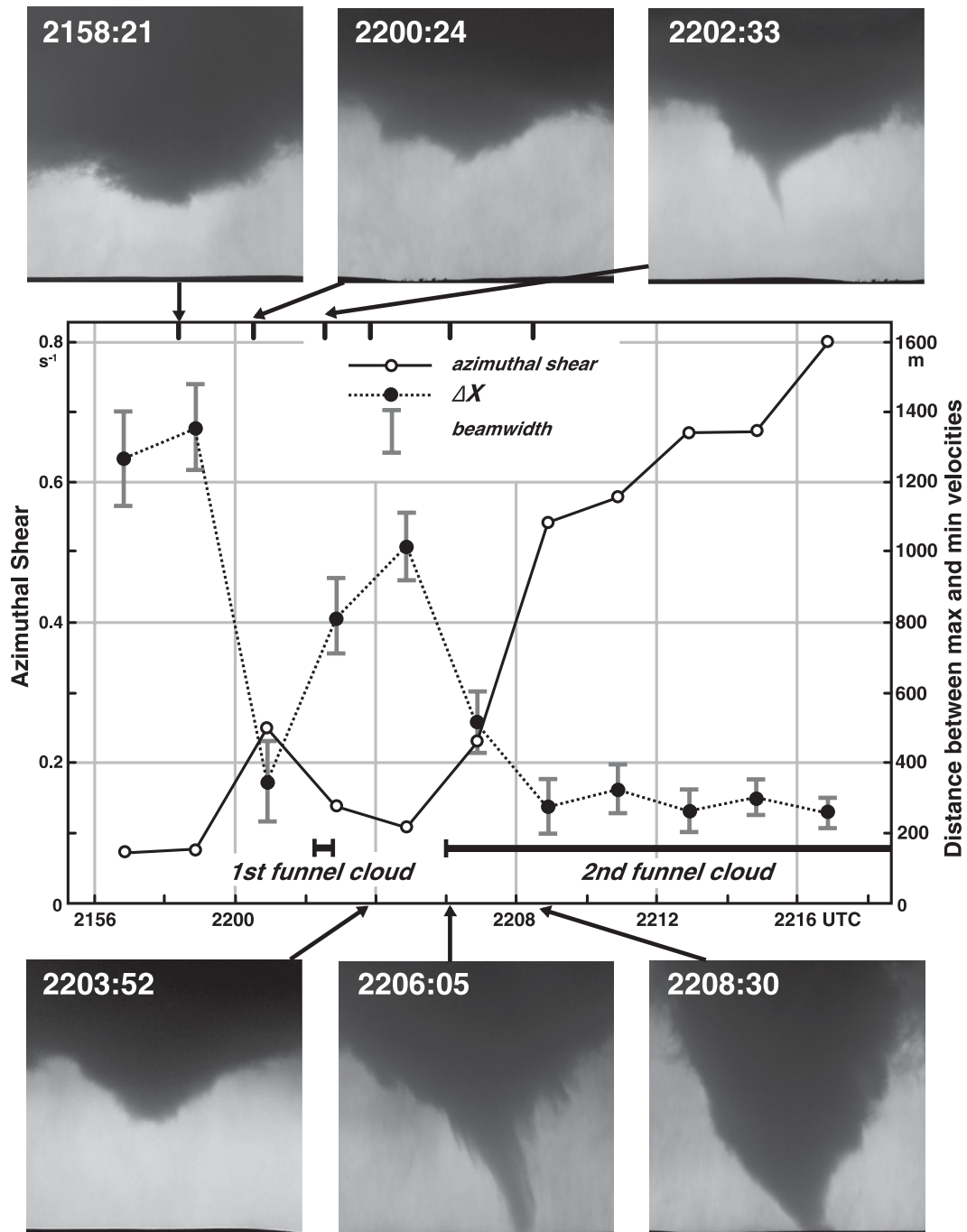


FIG. 3. Time plot of azimuthal shear (black line) and distance between the maximum and minimum radial velocities (dashed line) associated with the tornado based on measurements from DOW7. The beamwidth (in m) at the location of the tornado is also plotted. Photos taken from the DOW7 site are shown at 2158:21, 2200:24, 2202:33, 2203:52, 2206:05, and 2208:30 UTC. This is based on the scan at 0.5° . Times when two funnel clouds were observed are indicated. Photos were photogrammetrically enlarged or reduced so that the relative dimensions of the tornado can be estimated.

funnel aloft during this time. A time plot of vertical vorticity at low levels based on dual-Doppler wind syntheses (discussed in Part II of this series) also confirms the single-Doppler observations shown in the figure.

A second period of increased shear began at ~ 2205 UTC. A second funnel was observed to “touch” the ground by ~ 2206 UTC and was visible up until the tornado dissipated at ~ 2231 UTC. The azimuthal shear continued to increase

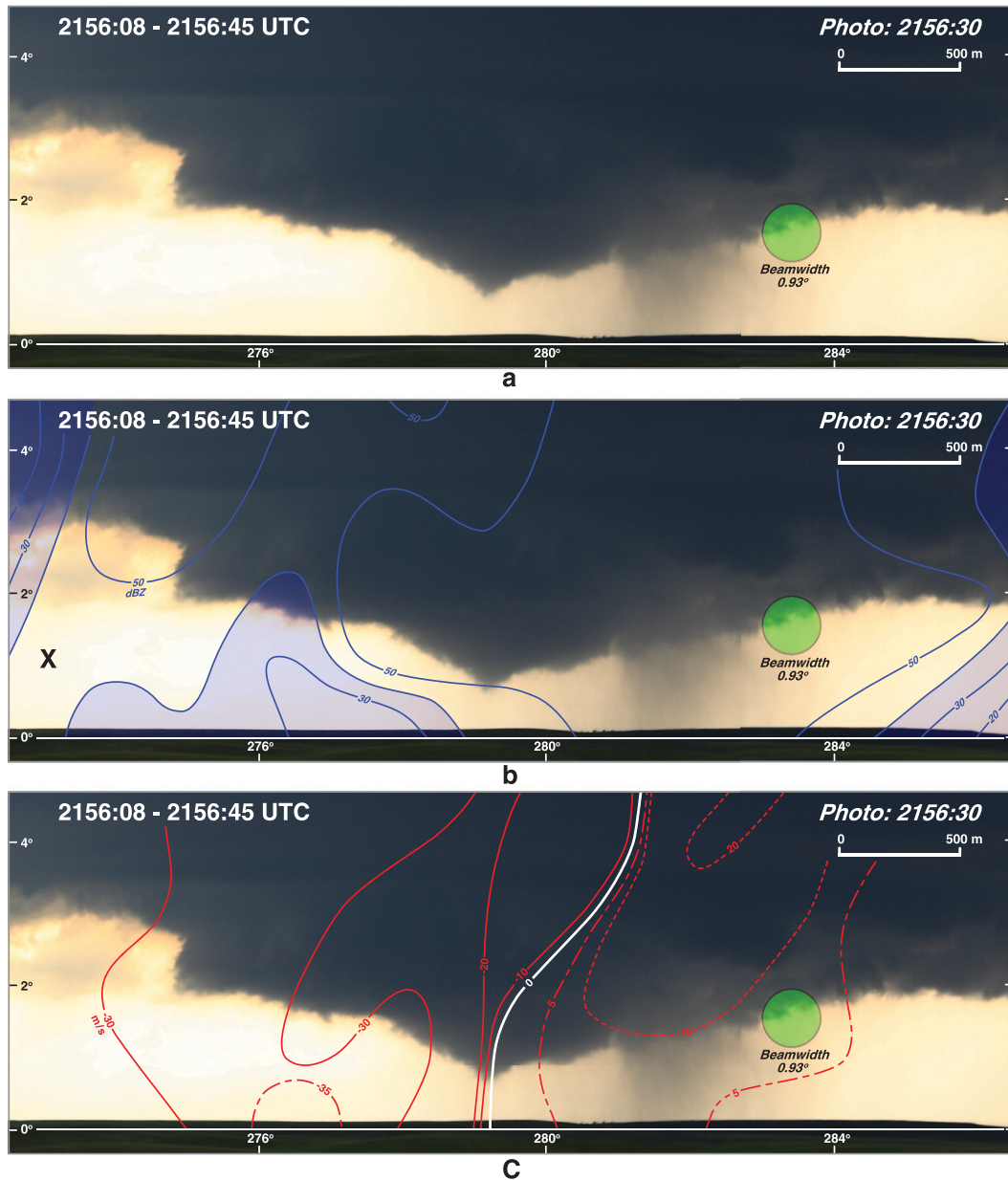


FIG. 4. (a)–(c) Wide-angle photograph of the LaGrange tornado at 2156:30 UTC. Blue lines in (b) are isopleths of radar reflectivity with values less than 40 dBZ are shaded light blue. Red lines in (c) are isopleths of single-Doppler velocity. Solid and dashed lines represent negative and positive velocities, respectively. Additional isopleths of Doppler velocities have been added (dash-dot lines) in weak gradient regions. The scales labeled in the figures are valid at the distance of the tornado. All wide-angle photographs (Figs. 4, 7, 9, 11, 12, 14, and 16) have been enlarged or reduced so that the scales are equivalent (i.e., the relative dimensions of the tornado are equal when comparing photographs shown in these figures). The letter “X” labeled in (b) is shown in Fig. 2a.

monotonically during this second phase. This increase may be partially attributed to improved resolution owing to the smaller beamwidth resolving higher radial velocities as the tornado approached the radar. There are two distinct trends of increased shear after ~ 2205 UTC. The first segment (2205–2209 UTC) is associated by both

a decrease in ΔX and an increase in outgoing and incoming radial velocities. This rapid intensification in shear is shown by the steep slope in Fig. 3. The second trend is not attributed to a contraction of the rotational couplet since the distance separating the maximum and minimum radial velocities remained relatively constant

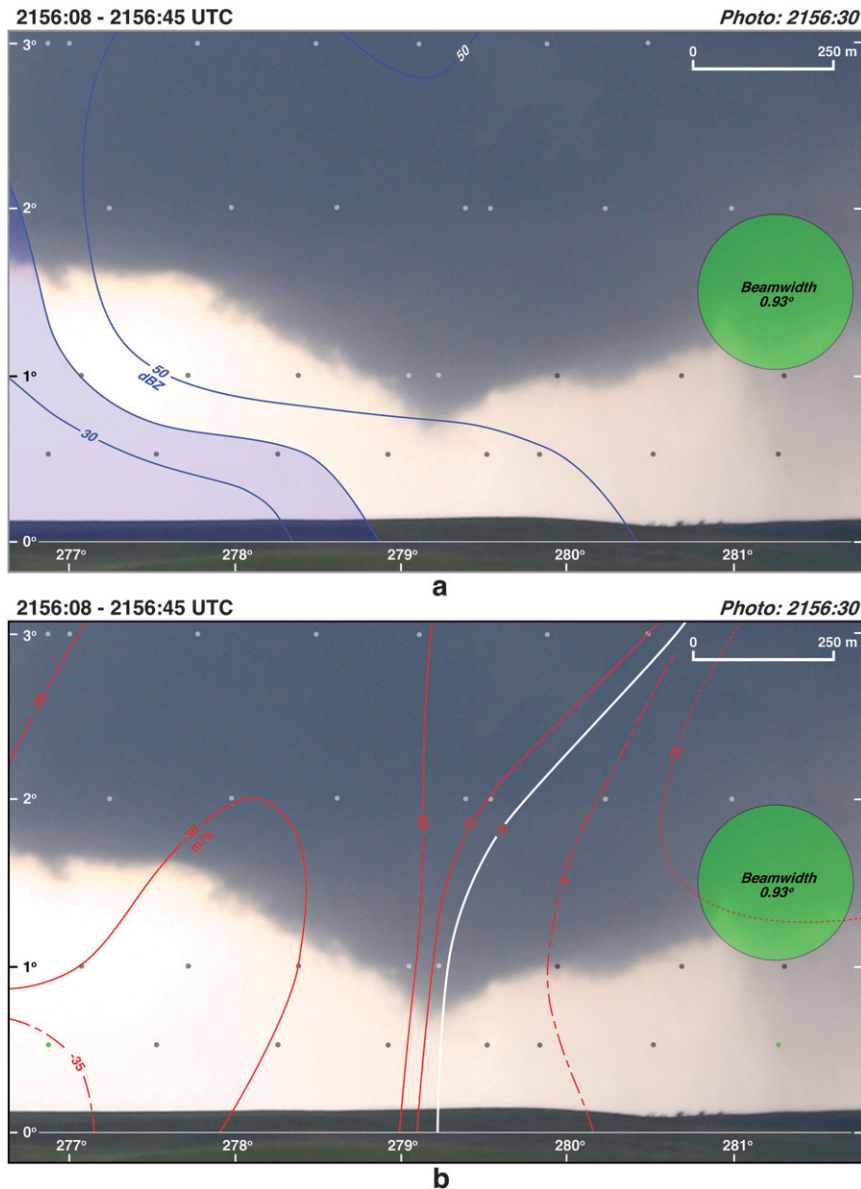


FIG. 5. (a),(b) Enlarged photograph of the LaGrange tornado at 2156:30 UTC. Blue lines in (a) are isopleths of radar reflectivity with values less than 40 dBZ are shaded light blue. Red lines in (b) are isopleths of single-Doppler velocity. Solid and dashed lines represent negative and positive velocities, respectively. Additional isopleths of Doppler velocities have been added (dash-dot lines) in weak gradient regions. The green circle represents the beamwidth of the radar. The scale labeled in the figures are valid at the distance of the tornado. All zoomed-in photographs (Figs. 5, 6, 8, 10, 13, 15, 17, 18, and 19) have been enlarged or reduced so that the scales are equivalent (i.e., the relative dimensions of the tornado are equal when comparing photographs shown in these figures). The small dots represent the raw data points from DOW7 and the small green dots represent the peak velocities used in Fig. 3.

after 2209 UTC. (It is possible, however, that the actual diameter of the vortex could be below the resolution of the radar data.) The slope of the azimuthal shear versus time is less during this period. The evolution of the first funnel cloud highlights the tenuous nature of using

visual observations to deduce the strength of the low-level azimuthal shear. The first indication of a developing WEH within the hook echo occurred at 2158 UTC and was clearly identifiable during the scan at 2200 UTC (Fig. 2).

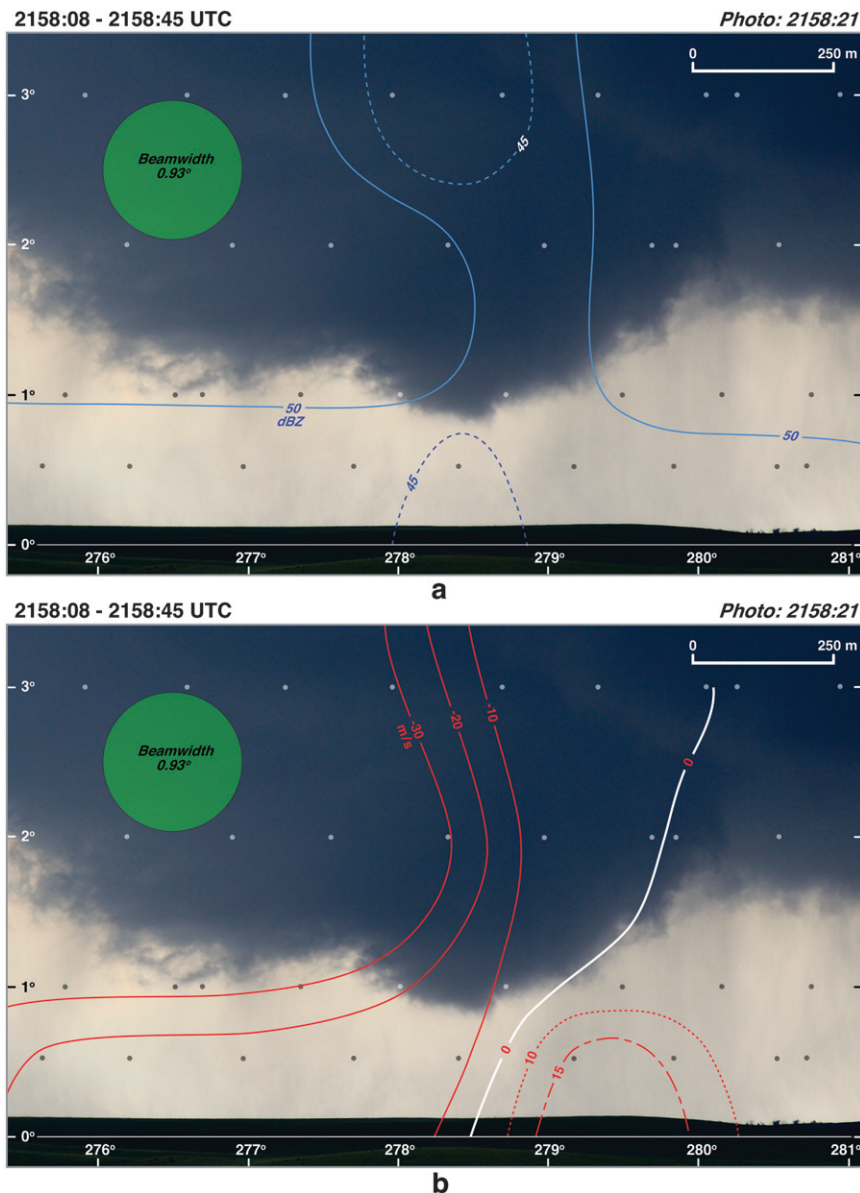


FIG. 6. Enlarged photograph of the LaGrange tornado at 2158:21 UTC. Contour description is the same as in Fig. 5.

5. Vertical cross sections through the tornado

The high-resolution radar data was combined with a series of still photographs in an attempt to document the evolution of the tornado’s visual structure in relation to the radar reflectivity and Doppler velocity fields. The range to the rotational couplet was determined using single-Doppler velocity data from DOW7. At these ranges, which in some cases varied by a few range gates at different elevation angles, pseudovertical cross sections were assembled through the center of the WEH and the rotational couplet. These cross sections are

along curved surfaces (i.e., constant range) as shown in Fig. 2. The first analysis time was at ~2156 UTC and the last analysis time was ~2217 UTC. Since the portion of the volume scans used in these analyses is ~30 s, the radar data are less correlated with the photographs for scans farthest removed from the time of the picture.

a. 2156:08–2156:45 UTC

Two series of cross sections were created for each radar volume scan. One was based on a wide-angle view of the visual features below the cloud base and a second

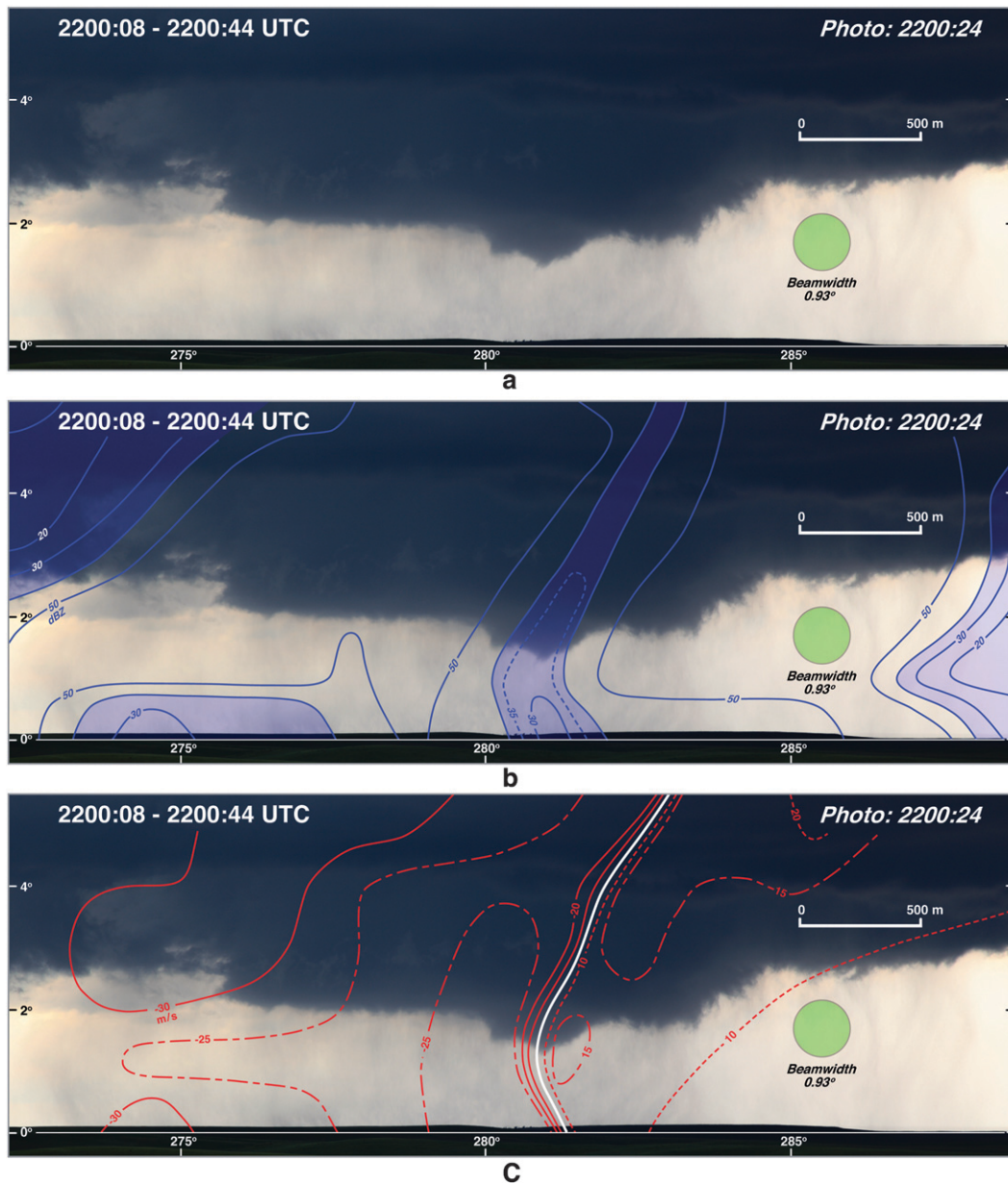


FIG. 7. Wide-angle photograph of the LaGrange tornado at 2200:24 UTC. Contour description is the same as in Fig. 4.

was a magnified view that would reveal the details of the developing and mature stages of the tornadic circulation. The wall cloud and a funnel aloft are apparent during the first volume scan at 2156:08–2156:45 UTC (Fig. 4). The southern edge (left in the picture) of the wall cloud was ~ 400 m below cloud base and the lower tip of the funnel was ~ 200 m above ground level (AGL). A visual rain shaft was located north of the funnel cloud (281° – 283° azimuth) and was embedded in radar reflectivity >50 dBZ. The funnel was centered near the

0 m s^{-1} isopleth of Doppler velocity (Fig. 4c).¹ The location of the curtain of precipitation that connects the hook echo with the main storm is shown (label “X”) in Figs. 2a and 4b. This curtain is positioned near the southern edge of the wall cloud (Fig. 4b) where precipitation

¹ The tornado-relative single-Doppler velocities can be approximated by adding $\sim 10 \text{ m s}^{-1}$ to the velocity field shown in Fig. 4b owing to the motion of the circulation toward the radar (9.1 – 9.6 m s^{-1}).

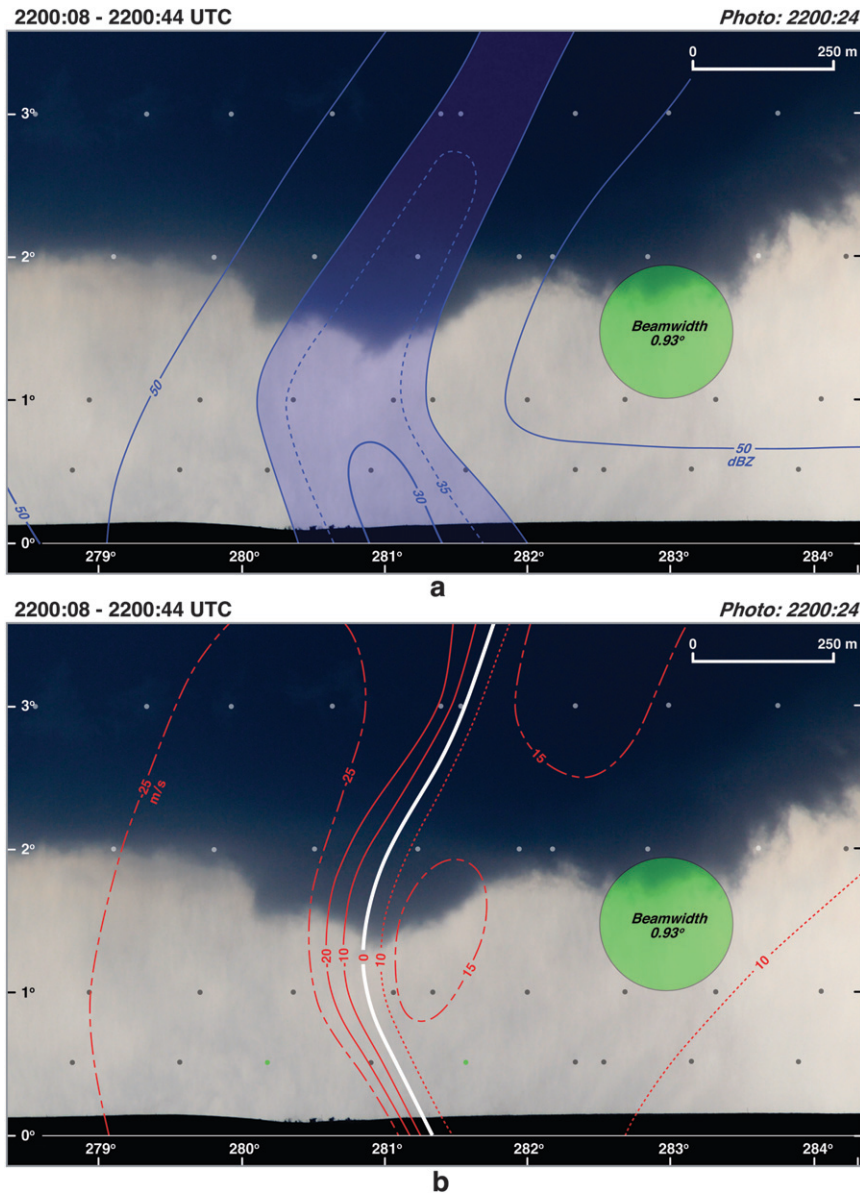


FIG. 8. Enlarged photograph of the LaGrange tornado at 2200:24 UTC. Contour description is the same as in Fig. 5.

was not visually apparent even though the values of radar reflectivity were between 40–50 dBZ. This observation suggests that the echo return could have been a result of a sparse collection of large hydrometeors.

An enlargement of the analysis at 2156:08–2156:45 UTC centered on the funnel cloud is shown in Fig. 5. The positions of the raw values of radar reflectivity and Doppler velocity are plotted as dots on the figure. The green dots at the 0.5° elevation angle represent the maximum/minimum values within the rotational couplet that were used to calculate the azimuthal shear shown in Fig. 3. The DOW7 radar beamwidth has been added to

all vertical cross sections shown in this section. Azimuthal oversampling resulted in horizontal spacing of the raw data less than the beamwidth.

b. 2158:08–2158:45 UTC

The first suggestion of the formation of a region of weak echo within the hook was observed during the 2158:08–2158:45 UTC volume scan (Fig. 6). The region is denoted by a vertical trough of radar reflectivities <50 dBZ. Two pockets of reflectivities <45 dBZ are evident in Fig. 6a. The horizontal gradients of single-Doppler velocities have increased (Fig. 6b), but they appear in two separate

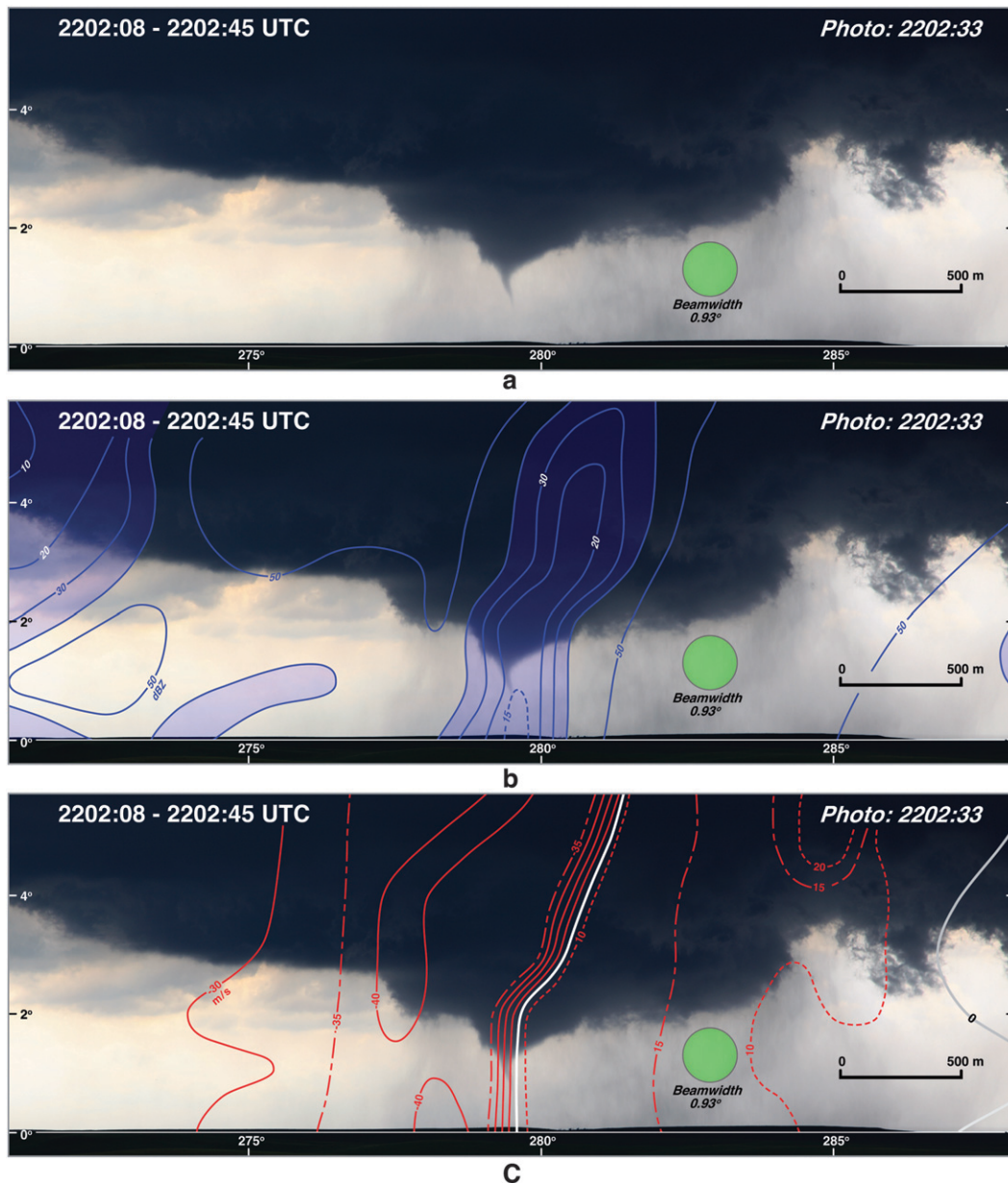


FIG. 9. Wide-angle photograph of the LaGrange tornado at 2202:33 UTC. Contour description is the same as in Fig. 4.

locations. One area is below the 1° elevation angle where the shear is strongest in the northern section of the weak-echo region while it occurs to the south at higher levels. The appearance of a weak-echo region before vortex-scale collapse and significant rotation intensifies (Fig. 3) is surprising and suggests that centrifuging of hydrometeors occurs more rapidly than previously suggested (Dowell et al. 2005).

c. 2200:08–2200:44 UTC

A WEH (qualitatively defined as the area <40 dBZ embedded within the circulation) was clearly evident by

the 2200:08–2200:44 UTC volume (Fig. 2b) and is tilting to the north with increasing height (Figs. 7b and 8a). The diameter of the WEH decreases with increasing height and the minimum values within the hole are near the surface (<30 dBZ). Precipitation can be seen within and extending beyond the wall cloud (Fig. 7). The tube of high reflectivity (>50 dBZ) that comprised the hook echo (Fig. 2c) approximately surrounds the wall cloud during this time (Fig. 7b). The WEH and the rotational couplet are centered on the lowered cloud feature pendant from the wall cloud (Figs. 7 and 8). The rotation

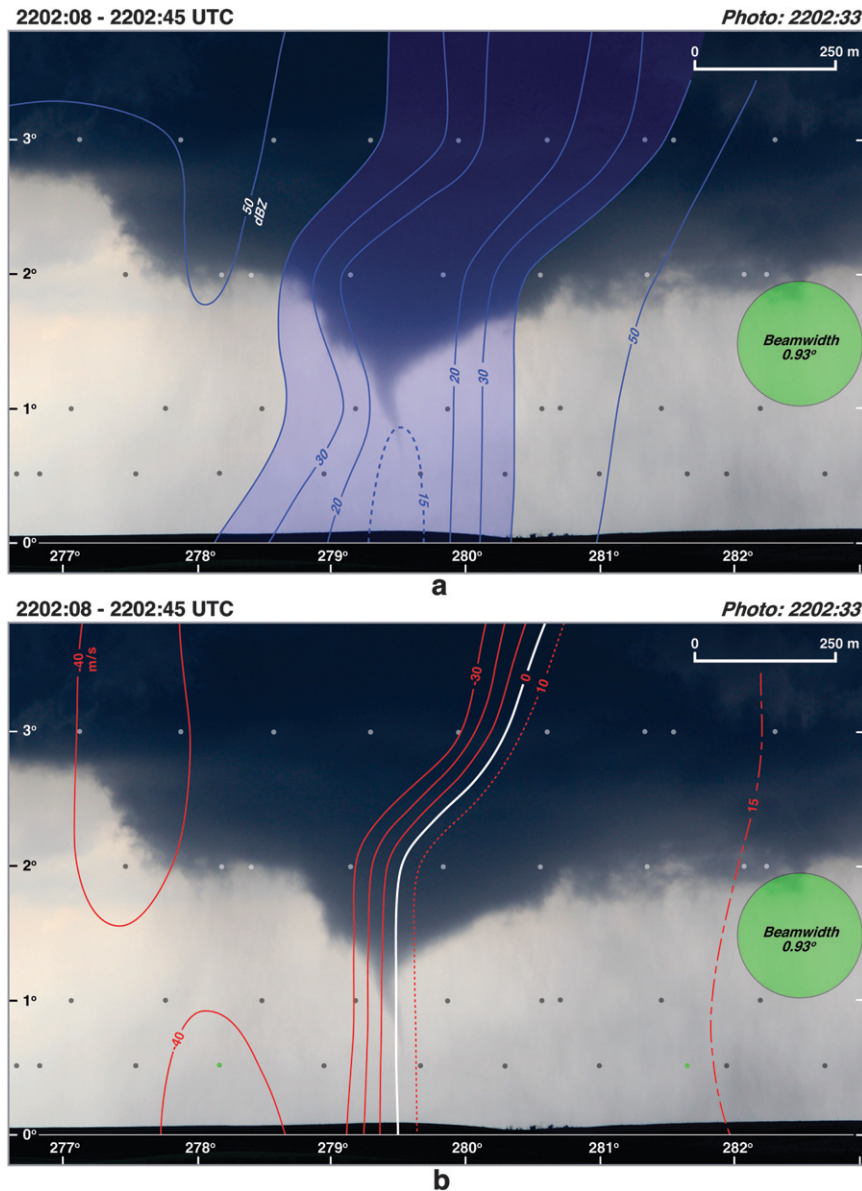


FIG. 10. Enlarged photograph of the LaGrange tornado at 2202:33 UTC. Contour description is the same as in Fig. 5.

has increased as measured by the azimuthal shear at low levels (0.25 s^{-1} ; Fig. 3) and the increased gradient of Doppler velocities shown in Figs. 7c and 8b.

d. 2202:08–2202:45 and 2204:08–2204:45 UTC

A narrow funnel cloud with a diameter of 30–40 m formed at 2202:33 UTC (Figs. 9 and 10). The WEH widened and minimum radar reflectivity values were still near the surface ($<15 \text{ dBZ}$). The asymmetry in single-Doppler velocities exhibited by the rotational couplet (Fig. 10b) is in large part owing to the translation of the tornado toward DOW7 mentioned earlier. The narrow funnel was

a transient feature and dissipated by the next volume scan (Fig. 11). The minimum radar reflectivity within the WEH remained near the surface, but the area $<15 \text{ dBZ}$ grew in depth to $\sim 450 \text{ m}$. Similar to the analysis presented in section 5c, the largest diameter of the WEH is near the surface and narrows with increasing height.

e. 2206:10–2206:46 and 2208:11–2208:47 UTC

The azimuthal shear began to increase dramatically after $\sim 2205 \text{ UTC}$ (Fig. 3) and was accompanied by the development of a second funnel cloud that reached the surface (Fig. 12). The visual appearance of the precipitation

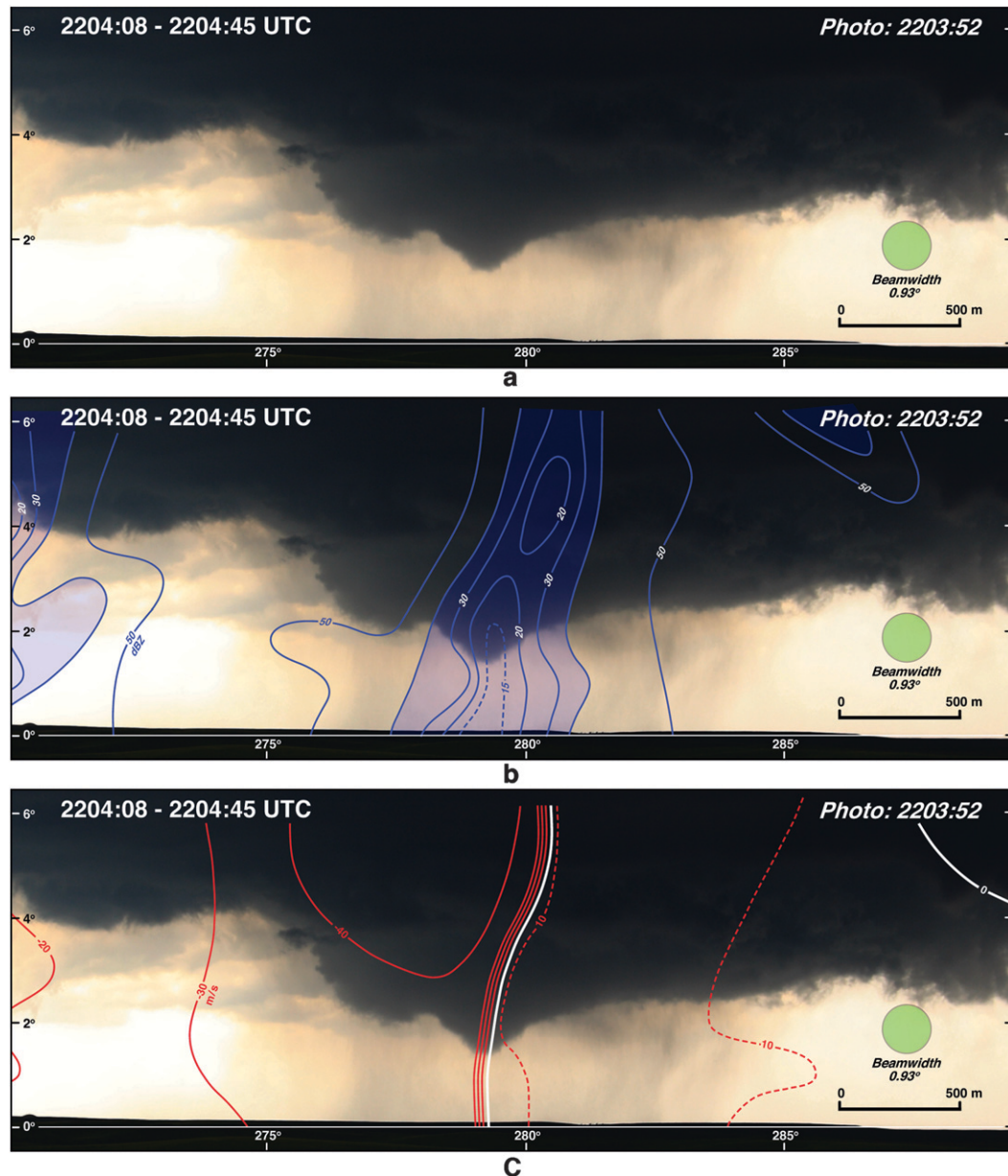


FIG. 11. Wide-angle photograph of the LaGrange tornado at 2203:52 UTC. Contour description is the same as in Fig. 4.

encompassing the funnel (Fig. 12) is consistent with the tube of high reflectivity surrounding the WEH (Figs. 2e and 12b). The diameter of the WEH (~ 600 m) was much larger than the funnel. The region of radar reflectivity < 15 dBZ extends to a higher altitude suggesting that centrifuging of hydrometeors increased owing to stronger rotation. A major structural change within the WEH near the surface has occurred during this time. The radar reflectivities are now greater than 20 dBZ and the minimum radar reflectivities denoted

by the 15-dBZ contour are now aloft (Figs. 12b and 13a). This increase in echo intensity at low levels may have been a result of lofted debris from the surface although none was visually apparent in the photograph. The strongest rotation associated with the tornado is concentrated in the lowest few hundred meters as indicated by the intense positive and negative values of Doppler velocity (Figs. 12c and 13b).

The funnel cloud and the WEH continue to increase in diameter by the 2208:11–2208:47 UTC volume scan

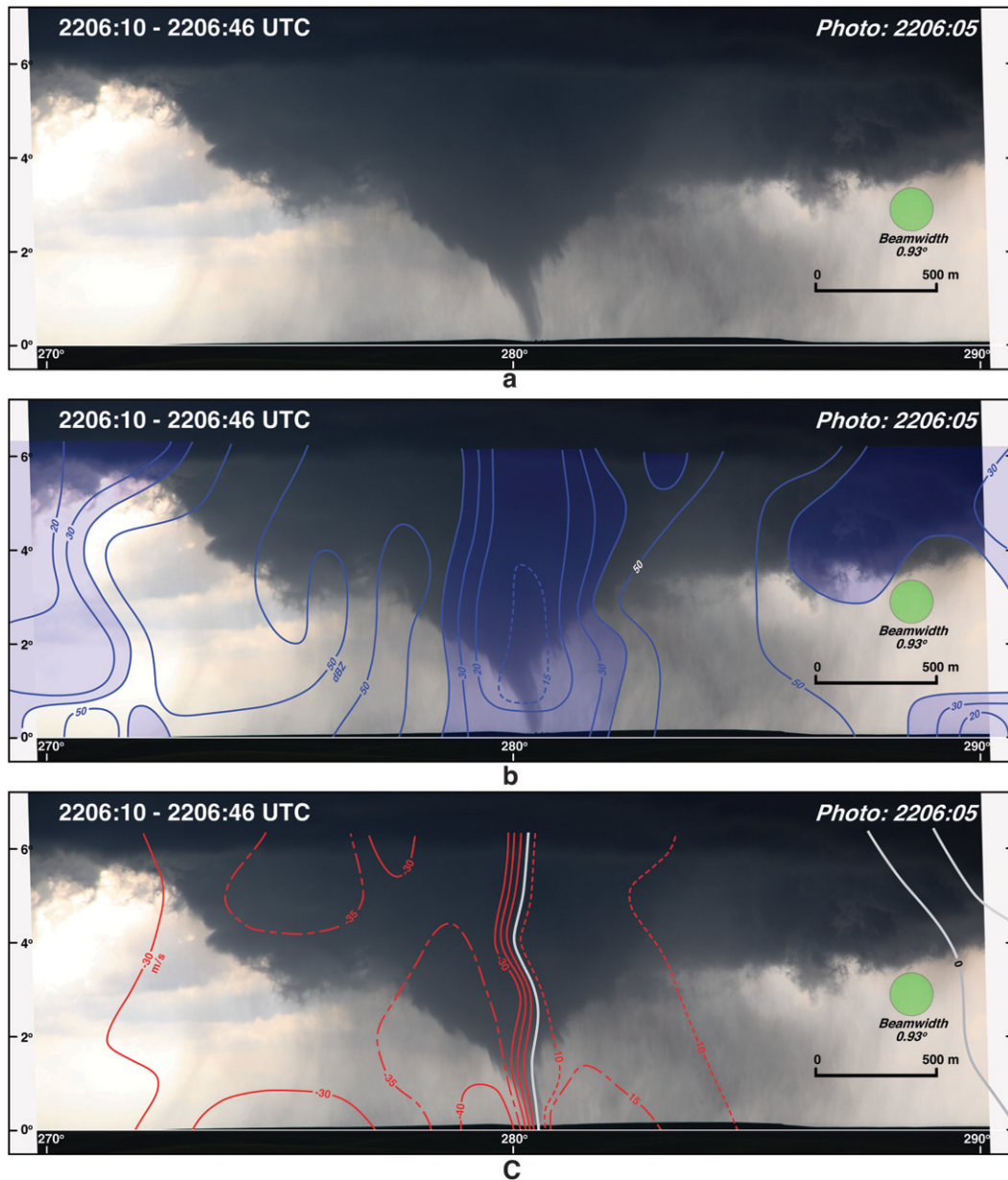


FIG. 12. Wide-angle photograph of the LaGrange tornado at 2206:05 UTC. Contour description is the same as in Fig. 4.

(Figs. 14 and 15). The vertical structure of the WEH is “pear shaped” (Figs. 14b and 15a) similar to the results presented by Bluestein et al. (2004) but different than the more “U shaped” profiles shown by Wurman et al. (1996b) and Wurman and Samaras (2004). The wide-angle photo taken at 2208:17 UTC (Fig. 14) highlights a discontinuity in the funnel cloud at ~200 m where it widens abruptly. It is possible that this visual feature demarcates the top of the strong inflow layer where convergence leads to intense rotation as suggested by depth of the rotational couplet in Fig. 14c. This discontinuity is less apparent in a zoomed-in

photograph taken a few seconds later at 2208:30 UTC (Fig. 15). The Doppler velocity analysis shown in Figs. 14c and 15b is the first to suggest the existence of a second rotational couplet aloft located within the cloud. This feature was also apparent during the 2210:10–2210:46 UTC scan volume (not shown). The decrease in rotational velocities at ~500 m between the low- and upper-level couplets may be related to air being forced radially outward from the tornado center at a location above the intense inflow as suggested by Bluestein et al. (2007a) and numerically simulated by Lewellen et al. (2000).

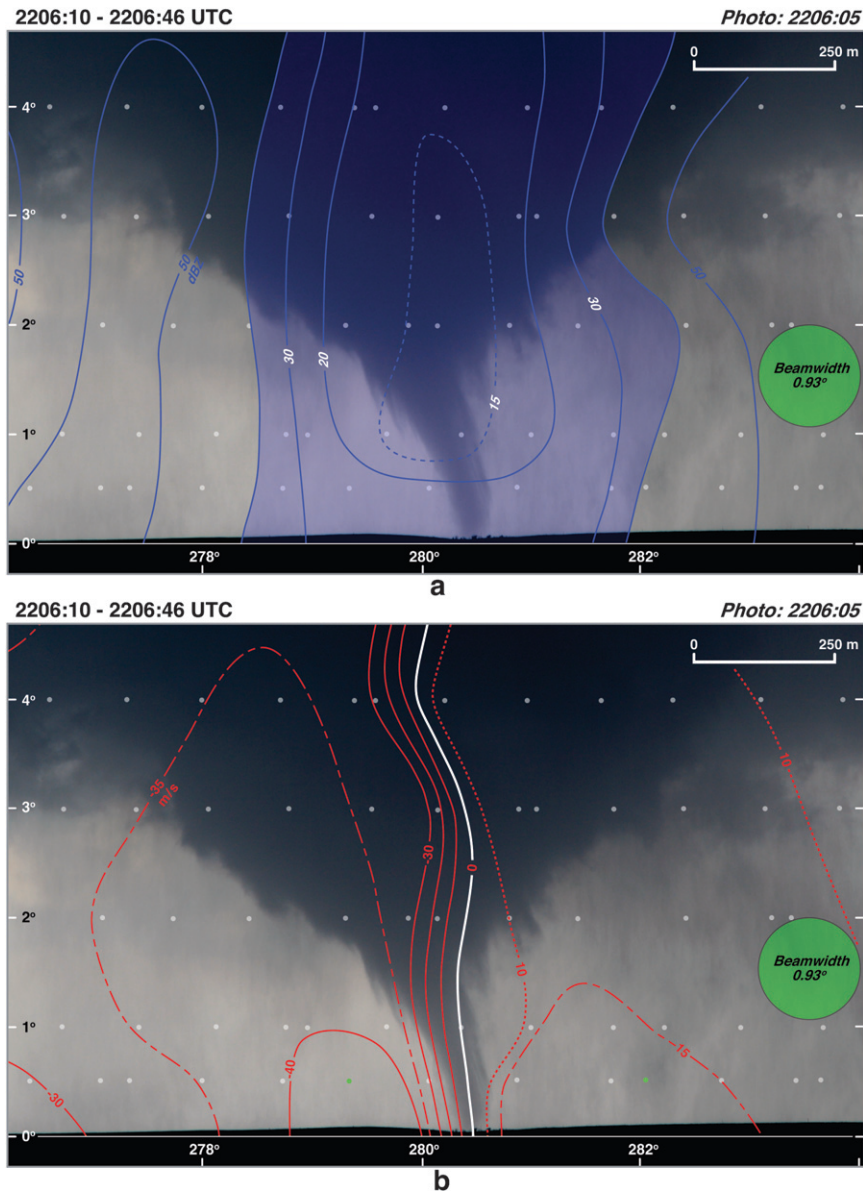


FIG. 13. Enlarged photograph of the LaGrange tornado at 2206:05 UTC. Contour description is the same as in Fig. 5.

*f. 2212:10–2212:46, 2214:09–2214:45, and
2216:08–2216:45 UTC*

The tornado is embedded in heavy precipitation as shown in the wide-angle photograph taken at 2211:58 UTC (Fig. 16).² There is good agreement between the precipitation seen in the photograph and the superimposed

² The contrast/brightness of the photos shown in Figs. 16–20 have been adjusted to highlight the condensation funnel structure. As a result, the contrast of the precipitation shaft may be reduced.

echo associated with the hook echo (Figs. 2h and 16b). Note the slope of the isopleths of radar reflectivity between 267° and 271° and the precipitation shaft in the same region. The increase of the radar reflectivity within the WEH at low levels has continued with echoes >45 dBZ centered at the location of the funnel (Figs. 16b and 17a). The resultant structure can be described as a couplet of high/low radar reflectivity in the vertical. This increase in echo return within the WEH with time can also be seen by comparing the low-level scans shown in Figs. 2f–j. Once again, this is suggestive of debris being lofted from the

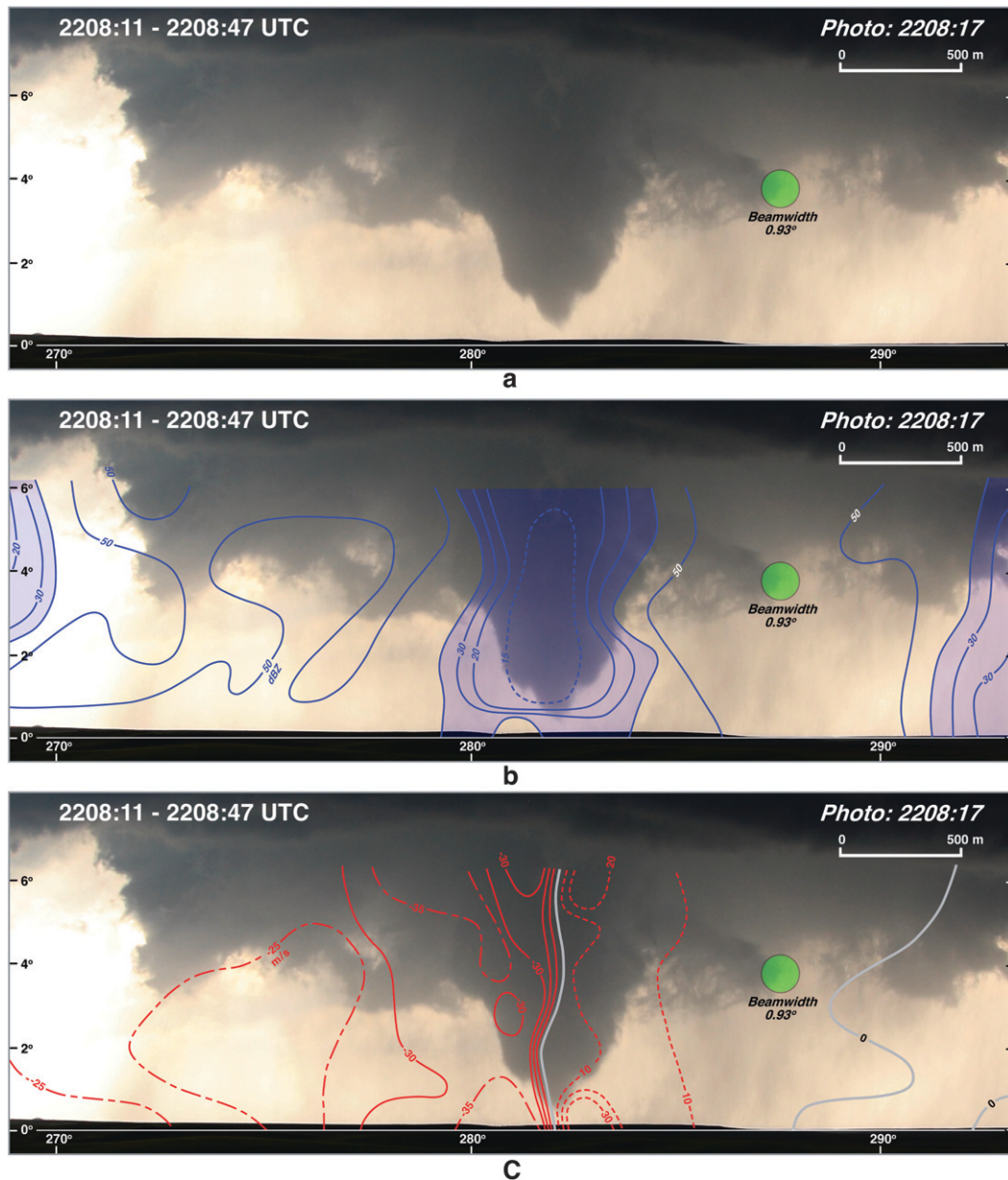


FIG. 14. Wide-angle photograph of the LaGrange tornado at 2208:17 UTC. Contour description is the same as in Fig. 4.

ground (debris does seem to be apparent from 281° to 282° in Fig. 17).

The rotational couplet at low levels continues to intensify with velocities now less than -50 m s^{-1} and greater than 30 m s^{-1} toward and away from the radar, respectively (Figs. 16c and 17b). The rotational speeds first decrease above this level before increasing in strength between 5° and 6° in elevation angle (Fig. 17b), similar to the velocity structure shown in the previous section. The near-surface structure of the WEH continues to evolve

and shows a tapered structure with weaker echoes (i.e., a trough) extending to the surface during the 2214:09–2214:45 UTC volume scan (Fig. 18a). Interestingly, a signature feature of the hook echo, as reported in the literature, is a tube of high reflectivity that is tapered at the bottom (e.g., Wurman and Gill 2000; Dowell et al. 2005). The results shown in Fig. 18a are the first analysis time when the region of high reflectivity exhibits a narrowing near the surface. It is possible that the tornado was moving over a region that was devoid of debris scatterers during this

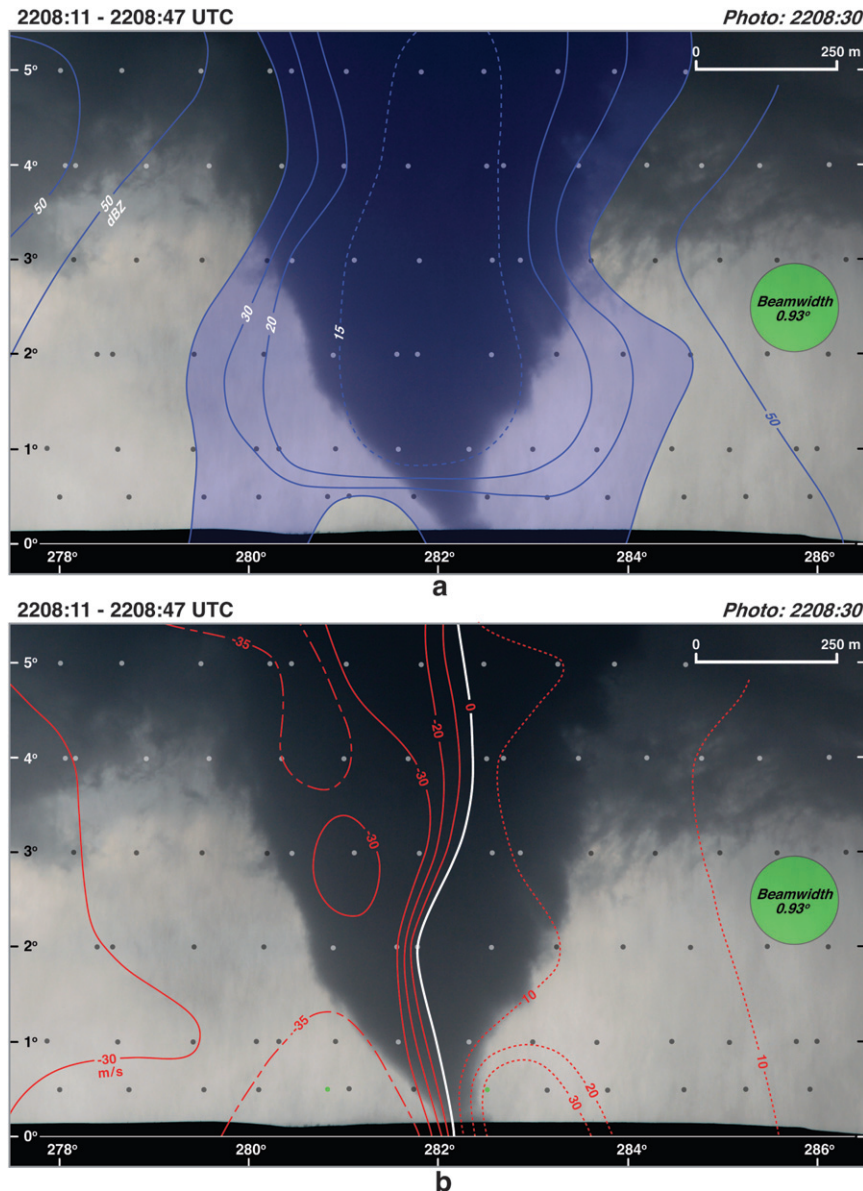


FIG. 15. Enlarged photograph of the LaGrange tornado at 2208:30 UTC. Contour description is the same as in Fig. 5.

time. Centrifuging would result in the axis of weak echoes extending to the surface. The rotational speeds continue to increase with Doppler velocities toward the radar less than -60 m s^{-1} (Fig. 18b). The strongest velocities were continuously recorded outside of the visible condensation funnel at the lowest elevation angle for all analysis times.

The echo structure changes again during the next volume scan (2216:08–2216:45 UTC). Higher radar reflectivities $>45 \text{ dBZ}$ were centered on the funnel cloud at lowest levels suggesting the presence of debris particles (Fig. 19a). The area encompassed by the 45-dBZ

isopleth is 500 m wide and is surrounded by an annulus of weaker echoes seen at 270° and 279°. This is the time that the hook began to exhibit a double-ring structure that is discussed in more detail in the next section. The two intense rotational couplets in the vertical are prominent features in Fig. 19b. One of the couplets is located near the surface and the other is located between the 4° and 5° elevation angles. To the authors' knowledge there have been three other case studies that have shown rotational couplets near the surface and aloft associated with a tornado (Wurman and Gill 2000; Dowell et al. 2005; Kosiba et al. 2008).

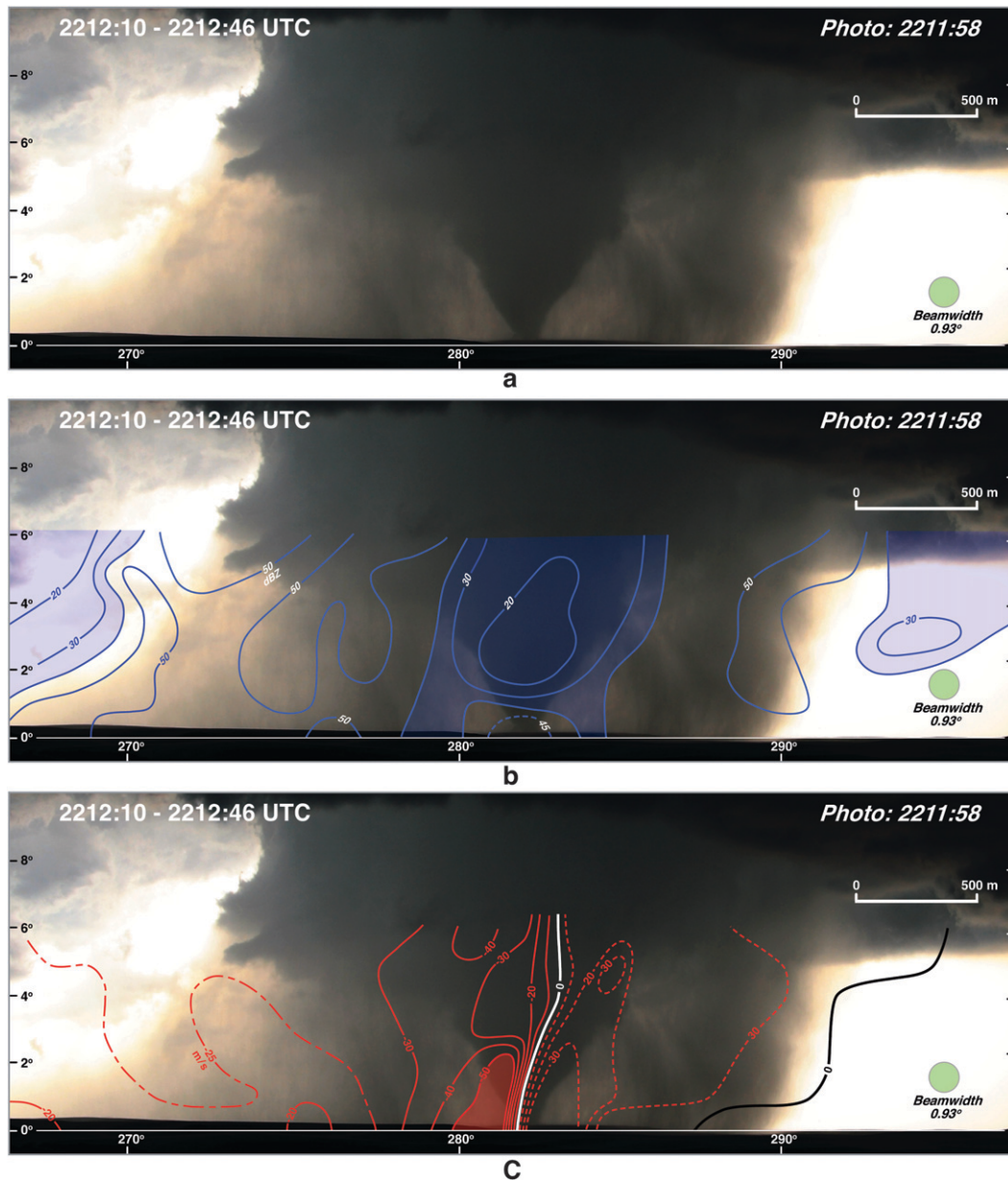


FIG. 16. Wide-angle photograph of the LaGrange tornado at 2211:58 UTC. Contour description is the same as in Fig. 4. Radial velocities less than -50 m s^{-1} are shaded light red.

g. Double-ring structure within the hook echo

Wurman et al. (1996a,b) and Wurman and Gill (2000) were among the first to report a double-ring structure within a hook echo. They proposed that the inner ring was associated with debris lofted from the ground while the outer ring was associated with precipitation. Additional reports in the literature of a double-ring structure include Wurman et al. (2007a), Tanamachi et al. (2007), and Kosiba et al. (2008). Bluestein et al. (2007b) used

dual-polarization measurements at the X band to show convincing evidence that the inner ring of a hook echo was likely the result of debris particles.

DOW7 recorded a double-ring structure in the low-level scans of the LaGrange tornado during 2216:51–2217:06 UTC (Fig. 20a). The scan at 2° clearly shows an inner ring with a small WEH embedded within the larger hook echo and the funnel cloud. The small WEH is not apparent at 0.5° . The velocity differential across the tornado was $\sim 105 \text{ m s}^{-1}$ at this time (Fig. 20d). The

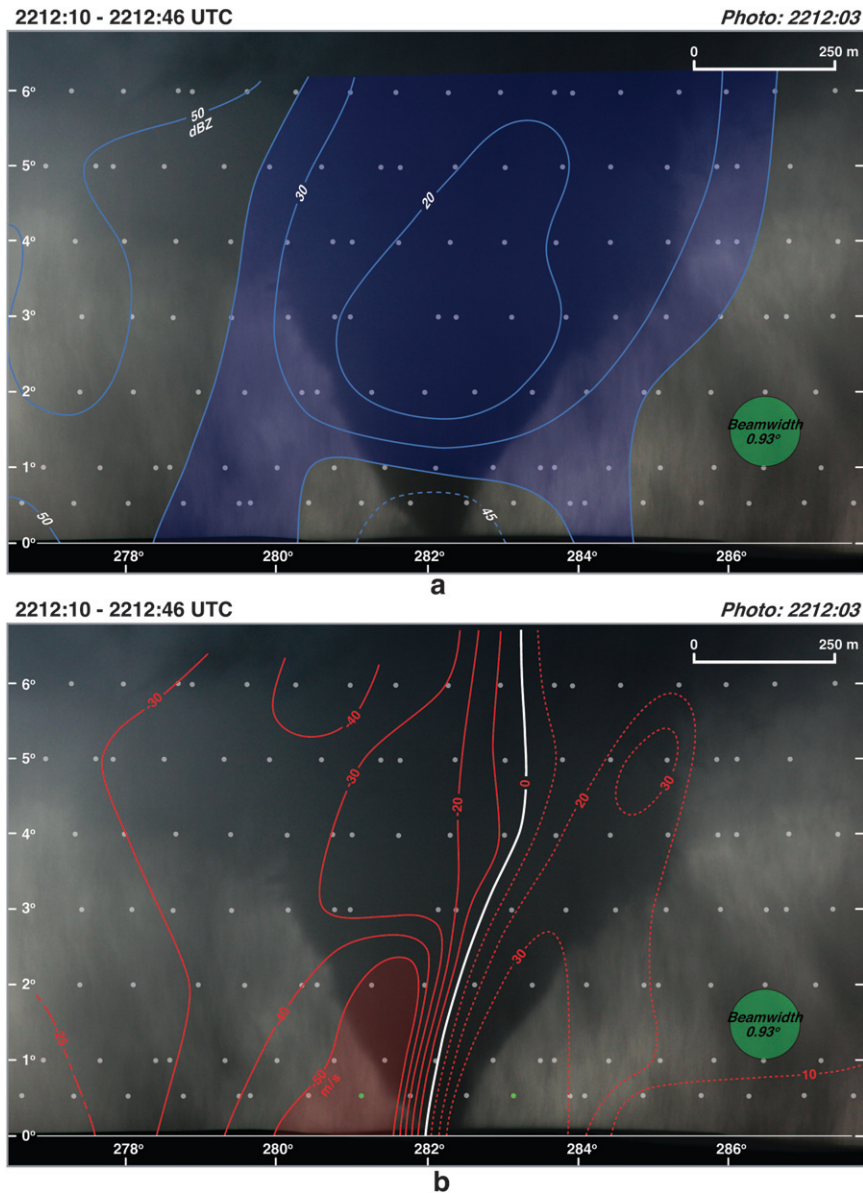


FIG. 17. Enlarged photograph of the LaGrange tornado at 2212:03 UTC. Contour description is the same as in Fig. 5. Radial velocities less than -50 m s^{-1} are shaded light red.

weak-echo trench surrounding the inner ring is denoted by the letter identifiers in Figs. 20a,c. There is a reduction in the diameter of this trench with increasing height (the radar did not scan the tornado at elevation angles greater than 3° during this volume).³ It appears that debris visually apparent between 272° and 278° (Fig. 20b) is associated with radar reflectivities $>45 \text{ dBZ}$. The

possible existence of lofted debris based on an examination of the high-definition video was inconclusive. Dowell et al. (2005) proposed that lofted debris and hydrometeors exhibit outward motion within a matter of a few tens of seconds. This results in a decrease in their number concentration within the tornado core (i.e., the appearance of a WEH) and increases their concentration somewhat outside the core. This scenario would describe the echo pattern shown in Fig. 20c. It is instructive to compare the radar reflectivities at 2° with those observed during the previous volume (shown in Fig. 19). The minimum dBZ values within the WEH in

³ An inspection of the next radar volume scan that started at 2218:08 UTC confirmed that the double-ring structure did not extend to the 3° elevation angle.

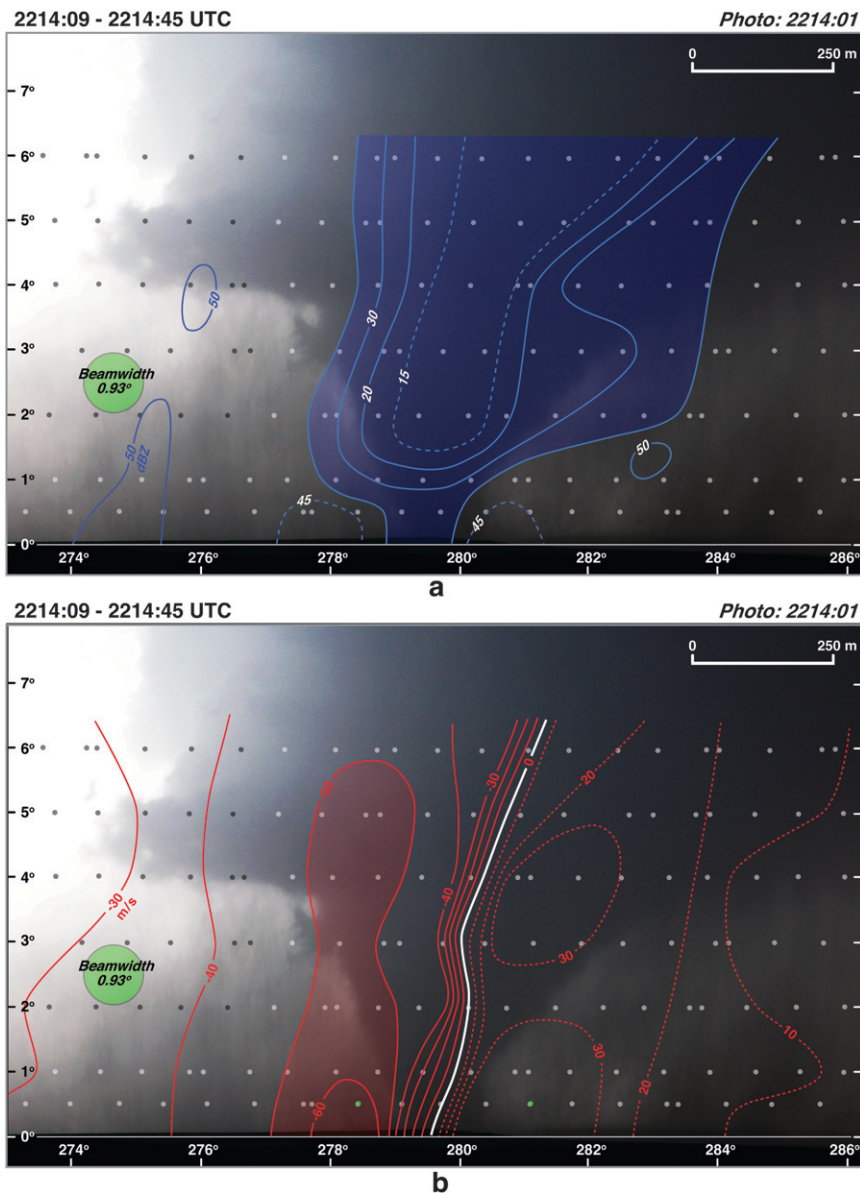


FIG. 18. Enlarged photograph of the LaGrange tornado at 2214:01 UTC. Contour description is the same as in Fig. 17.

Fig. 19 are <15 dBZ while they are <20 dBZ in Fig. 20. This suggests that some debris is present near the center axis of rotation at the later time.

6. Summary and conclusions

The current study presents a single-Doppler radar analysis combined with cloud photography of the LaGrange tornado on 5 June 2009 in an attempt to relate the hook echo, weak-echo hole (WEH), and rotational couplet to the visual characteristics of the tornado. The DOW radars set up ahead of the supercell storm

along a north–south highway. The radars collected high-resolution data on the wall cloud and the tornado. The tornado damage was not extensive based on a poststorm survey and led to an EF2 rating. Tornadogenesis is believed to have occurred at 2152 UTC based on the confirmed tornadic damage at the ground combined with the single-Doppler velocities within the rotational couplet observed by the DOW radar. The circulation at low levels went through two intensification periods based on azimuthal shear measurements. The first intensification was followed by the appearance of a brief funnel cloud. The second intensification was coincident with the appearance

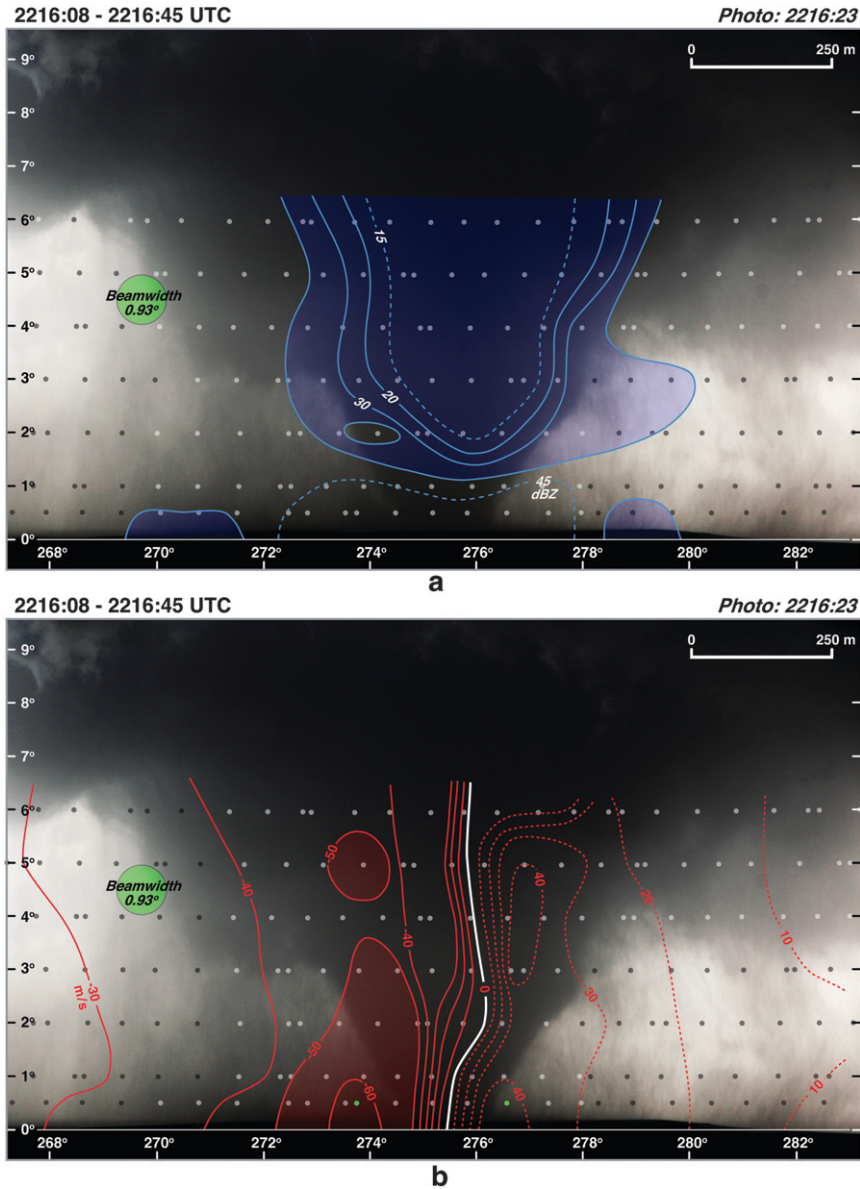


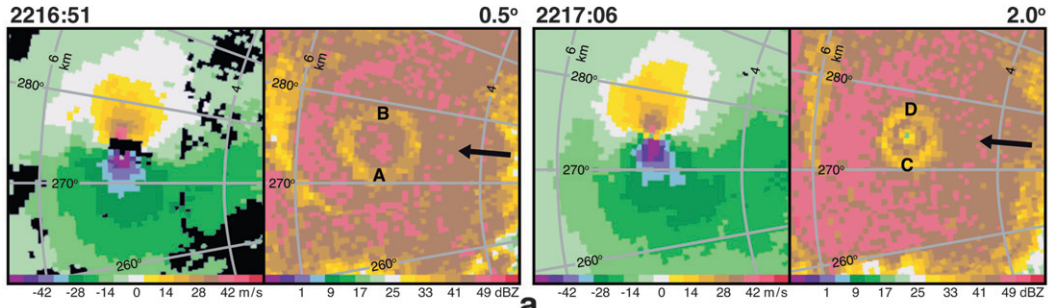
FIG. 19. Enlarged photograph of the LaGrange tornado at 2216:23 UTC. Contour description is the same as in Fig. 17.

of a second funnel cloud that remained in contact with the ground until the tornado dissipated.

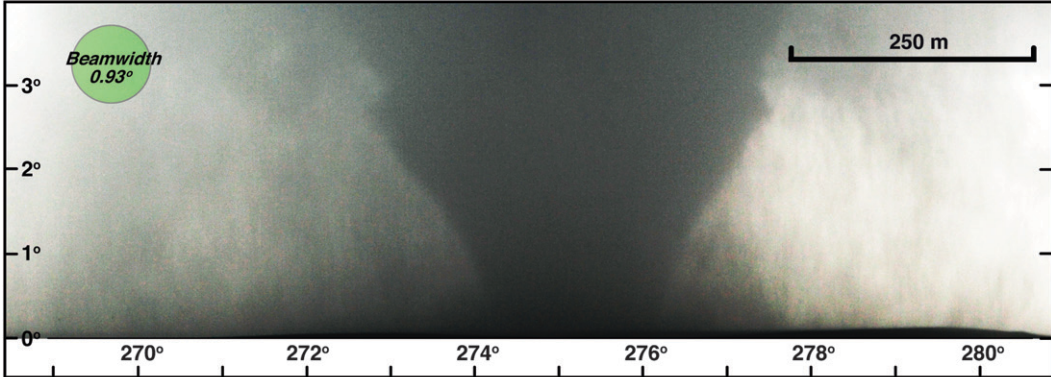
A weak-echo region within the hook echo formed at 2158 UTC and a WEH was clearly apparent by 2200 UTC

before the appearance of a funnel cloud. Dowell et al. (2005) proposed that a distinctive tornadic signature is the presence of a WEH within the hook and a tube of high reflectivity that is tapered near the surface. The

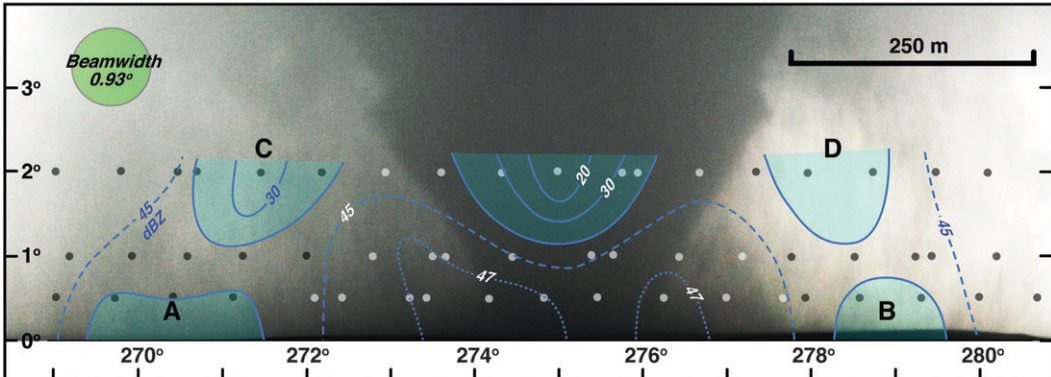
FIG. 20. (a) Low-level scans of Doppler velocity and radar reflectivity at 0.5° and 2° recorded by DOW7. (b) Photograph of the LaGrange tornado at 2216:41 UTC. (c) Radar reflectivity superimposed onto the photograph. Values less than 40 dBZ are shaded light blue. (d) Single-Doppler velocities superimposed onto the photograph. Solid and dashed lines represent negative and positive velocities, respectively. Values less than -50 m s^{-1} are shaded light red. The green circle represents the beamwidth of the radar. Letter identifiers denoting the position of the weak-echo region are plotted in (a) and (c). The scale labeled in the figures is valid at the distance of the tornado. The small dots represent the raw data points from DOW7.



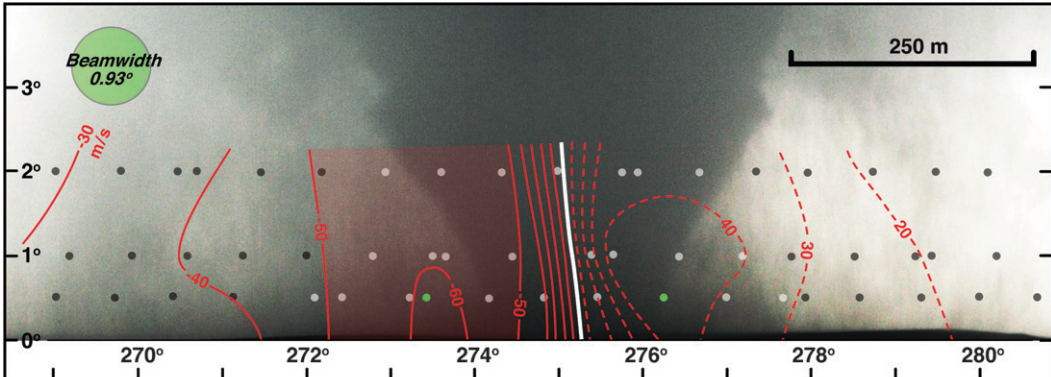
2216:51 - 2217:06 *Photo: 2216:41*



2216:51 - 2217:06 *Photo: 2216:41*



2216:51 - 2217:06 *Photo: 2216:41*



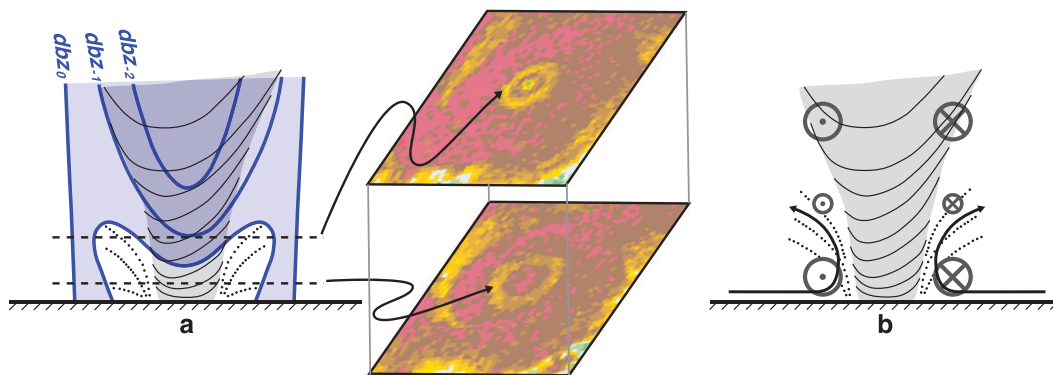


FIG. 21. Schematic models summarizing some of the observations from the LaGrange tornado. (a) Vertical profile of radar reflectivity through the inner ring of the hook echo. The black dashed lines represent the locations of scans through the tornado. Hypothetical low-level scans of radar reflectivity are shown by the two images on the right. Low values of radar reflectivity are shaded light blue. (b) Vertical profile of the tangential velocities. Strong rotational couplets are observed near the surface and aloft. Weaker velocities are observed in between and may be related to air being forced radially outward from the tornado center at a location above the intense inflow as shown by the black arrows.

tornado is often associated with higher reflectivity near the surface, consistent with Wurman et al. (1996a,b) among others. In contrast, Bluestein et al. (2004) described a pear-shaped echo structure near the surface. In addition, bulges in the WEH have been reported by Bluestein et al. (2007a).

The echo pattern through the hook echo on 5 June undergoes a dramatic evolution that appears to be different than these past investigations. Initially, the minimum radar reflectivities are near the surface (<15 dBZ) and the WEH does not suggest a tapered structure near the ground. Subsequently, higher reflectivities appear near the surface when the funnel cloud makes contact with the ground. During one analysis time, the increase of the radar reflectivity within the WEH at low levels results in a couplet of high/low radar reflectivity in the vertical. This increase in echo at low levels is believed to be associated with lofted debris although none was visibly apparent until the later analysis times. This observation is not surprising owing to the lack of damage indicators over the relatively barren terrain. The WEH was nominally wider than the visible funnel cloud.

The dataset provided the first detailed analysis of the double-ring structure within a hook echo that has been reported in several studies. The inner high-reflectivity region is believed to be a result of lofted debris. At higher elevation angles, a small WEH appeared within the high-reflectivity region owing to centrifuging of debris as schematically shown in Fig. 21a. Accordingly, both the inner and outer WEHs can be attributed to centrifuging.

A feature noted in past studies showing high-resolution vertical cross sections of single-Doppler velocity is an

intense couplet of negative and positive values in the lowest few hundred meters. This couplet was also evident in the analysis of the LaGrange tornado. The couplet was asymmetric with stronger negative velocities owing to the motion of the tornado toward the radar. However, another couplet indicating strong rotation was also noted aloft in a number of volume scans. The decrease in rotational velocities between the low- and upper-level couplets may be related to air being forced radially outward from the tornado center at a location above the intense inflow as summarized in Fig. 21b.

The results presented in this paper are based on data collected during year one of VORTEX2. Part II of this series of papers will compare the evolution of the dual-Doppler wind fields with the visual characteristics of the tornado. Data collected with a passive phased array radar, the Rapid-Scan DOW (Wurman et al. 2008) in the LaGrange tornado are in the process of being analyzed. In the second year of the field experiment it is hoped to collect high-resolution data using the DOWs rapid-scan phased array radars, and the recently installed dual-polarization capability. The latter would substantially aid in the interpretation of lofted debris as shown by Bluestein et al. (2007b). This information combined with detailed aerial and ground damage surveys will advance our understanding of the low-level structure of tornadoes.

Acknowledgments. Comments from two anonymous reviewers significantly improved an earlier version of the manuscript. The National Center for Atmospheric Research is sponsored by the National Science Foundation. Any opinions, findings, and conclusions or recommendations expressed in this publication are those of

the authors and do not necessarily reflect the views of the National Science Foundation. Research results presented in this paper were supported by the National Science Foundation under Grants ATM-0757714. The DOW radars are National Science Foundation Lower Atmospheric Observing Facilities supported by Grant ATM-0734001. The DOW deployments in VORTEX2 have been supported by Grants ATM-0910737 and ATM-0966095. Analysis of DOW data has been supported by Grant ATM-0947235. VORTEX2 has been supported, in part, by Grant ATM-0724318.

APPENDIX

Cloud Photogrammetry

The focal length of the lens for the wide-angle and zoomed images was 24 and 105 mm, respectively. A 360° panorama was taken from the photo site. The azimuth angles from the site to several landmarks were calculated using GPS and U.S. Geological Survey (USGS) topographic maps. These landmarks were identified on the panorama and also on the individual photographs of the wall cloud and tornado. An azimuth- and elevation-angle grid was calculated based on the known focal length and azimuth angles to the landmarks. These derived azimuth angles were within 0.1°–0.2° of the known landmarks. The distance to the tornado for the photos shown in this paper ranged from 5 to 17 km. The photographer was positioned within a few meters of the radar dish to minimize the azimuth-angle errors owing to the photo site not being collocated with the radar.

Wide-angle photos can be characterized by significant distortion at the corners of an image. This effect was minimized by the quality of the camera lens and limiting the analysis region presented in the figures to, at most, 40% of the total image size. This region was also located in the center of the photo. Accordingly, the areas of the photograph that might be expected to experience the most distortion were excluded. The time interval between photographs was variable but the average was ~12 s. To capture the evolution of the condensation funnel that can change significantly over a few seconds a high-definition video was also recorded at the same location. Important changes in the condensation funnel cloud are noted in the manuscript (e.g., differences highlighted in Figs. 14 and 15).

The motion of the tornado can introduce errors in the analyses even if the elapsed time for the radar scans is ~30 s. To correct for this effect, the radar data was shifted using a time–space conversion based on the tornado motion in the plane of the photograph. The time of the photograph was used as the analysis time.

Difficulties often encountered when comparing storm-intercept photographs are the different camera locations, focal length of the lens, and varying distances to the tornado. These factors can lead to erroneous perceived changes in the funnel width, for example. The superimposed photogrammetric angles on the pictures and the exact radial distance to the tornado based on the radar data provided a solution to this problem. This information was used to either enlarge or reduce the pictures so that the relative dimensions of the tornado were equal as shown in Fig. 1 and other figures presented in this manuscript (e.g., Figs. 3; Figs. 4, 7, 9, 11, 12, 14, and 16; Figs. 5, 6, 8, 10, 13, 15, 17, 18, and 19). These adjustments allow for a direct comparison of the tornado dimensions between photos. The largest condensation funnel width at 2209:58 UTC was ~600 m just below cloud base in Fig. 1.

REFERENCES

- Abrams, T., 1952: *The Manual of Photogrammetry*. George Banta Publishing, 876 pp.
- Alexander, C. R., and J. Wurman, 2005: The 30 May 1998 Spencer, South Dakota, storm. Part I: The structural evolution and environment of the tornadoes. *Mon. Wea. Rev.*, **133**, 72–96.
- Bluestein, H. B., J. G. LaDue, H. Stein, D. Speheger, and W. P. Unruh, 1993: Doppler radar wind spectra of supercell tornadoes. *Mon. Wea. Rev.*, **121**, 2200–2221.
- , W. P. Unruh, D. C. Dowell, T. A. Hutchinsohn, T. M. Crawford, A. C. Wood, and H. Stein, 1997: Doppler radar analysis of the Northfield, Texas, tornado of 25 May 1994. *Mon. Wea. Rev.*, **125**, 212–230.
- , W.-C. Lee, M. Bell, C. C. Weiss, and A. L. Pazmany, 2003: Mobile Doppler radar observations of a tornado in a supercell near Bassett, Nebraska, on 5 June 1999. Part II: Tornado-vortex structure. *Mon. Wea. Rev.*, **131**, 2968–2984.
- , C. C. Weiss, and A. L. Pazmany, 2004: The vertical structure of a tornado near Happy, Texas, on 5 May 2002: High-resolution, mobile, W-band, Doppler radar observations. *Mon. Wea. Rev.*, **132**, 2325–2337.
- , —, M. M. French, E. M. Holthaus, R. L. Tanamachi, S. Frasier, and A. L. Pazmany, 2007a: The structure of tornadoes near Attica, Kansas, on 12 May 2004: High-resolution, mobile, Doppler radar observations. *Mon. Wea. Rev.*, **135**, 475–506.
- , M. M. French, R. L. Tanamachi, S. Frasier, K. Hardwick, F. Junyent, and A. L. Pazmany, 2007b: Close-range observations of tornadoes in supercells made with a dual-polarization, X-band, mobile Doppler radar. *Mon. Wea. Rev.*, **135**, 1522–1543.
- Brown, R. A., L. R. Lemon, and D. W. Burgess, 1978: Tornado detection by pulsed Doppler radar. *Mon. Wea. Rev.*, **106**, 29–38.
- Dowell, D. C., C. R. Alexander, J. M. Wurman, and L. J. Wicker, 2005: Centrifuging of hydrometeors and debris in tornadoes: Radar-reflectivity patterns and wind-measurement errors. *Mon. Wea. Rev.*, **133**, 1501–1524.
- Forbes, G. S., 1981: On the reliability of hook echoes as tornado indicators. *Mon. Wea. Rev.*, **109**, 1457–1466.
- Fujita, T. T., 1981: Tornadoes and downbursts in the context of generalized planetary scales. *J. Atmos. Sci.*, **38**, 1511–1534.
- Holle, R. L., 1986: Photogrammetry of thunderstorms. *Thunderstorms: A Social and Technological Documentary*, 2nd ed. E. Kessler, Ed., Vol. 3, University of Oklahoma, 77–98.

- Kosiba, K. A., R. J. Trapp, and J. Wurman, 2008: An analysis of the axisymmetric three-dimensional low level wind field in a tornado using mobile radar observations. *Geophys. Res. Lett.*, **35**, L05805, doi:10.1029/2007GL031851.
- Lewellen, D. C., W. S. Lewellen, and J. Xia, 2000: The influence of a local swirl ratio on tornado intensification near the surface. *J. Atmos. Sci.*, **57**, 527–544.
- Malkus, J., 1952: The slopes of cumulus clouds in relation to external wind shear. *Quart. J. Roy. Meteor. Soc.*, **78**, 530–542.
- Rasmussen, E. N., and J. M. Straka, 2007: Evolution of low-level angular momentum in the 2 June 1995 Dimmitt, Texas, tornado cyclone. *J. Atmos. Sci.*, **64**, 1365–1378.
- , R. Davies-Jones, and R. L. Holle, 2003: Terrestrial photogrammetry of weather images acquired in uncontrolled circumstances. *J. Atmos. Oceanic Technol.*, **20**, 1790–1803.
- Stout, G. E., and F. A. Huff, 1953: Radar records Illinois tornadogenesis. *Bull. Amer. Meteor. Soc.*, **34**, 281–284.
- Tanamachi, R. L., H. B. Bluestein, W.-C. Lee, M. Bell, and A. Pazmany, 2007: Ground-based velocity track display (GBVTD) analysis of W-band Doppler radar data in a tornado near Stockton, Kansas, on 15 May 1999. *Mon. Wea. Rev.*, **135**, 783–800.
- Wakimoto, R. M., and B. E. Martner, 1992: Observations of a Colorado tornado. Part II: Combined photogrammetric and Doppler radar analysis. *Mon. Wea. Rev.*, **120**, 522–543.
- , W.-C. Lee, H. B. Bluestein, C.-H. Liu, and P. H. Hildebrand, 1996: ELDORA observations during VORTEX 95. *Bull. Amer. Meteor. Soc.*, **77**, 1465–1481.
- , H. V. Murphey, D. C. Dowell, and H. B. Bluestein, 2003: The Kellerville tornado during VORTEX: Damage survey and Doppler radar analyses. *Mon. Wea. Rev.*, **131**, 2197–2221.
- Wurman, J., 2001: The DOW mobile multiple-Doppler network. Preprints, *30th Int. Conf. on Radar Meteorology*, Munich, Germany, Amer. Meteor. Soc., P3.3.
- , and S. Gill, 2000: Finescale radar observations of the Dimmitt, Texas (2 June 1995), tornado. *Mon. Wea. Rev.*, **128**, 2135–2164.
- , and T. Samaras, 2004: Comparison of in-situ pressure and DOW Doppler winds in a tornado and RHI vertical slices through 4 tornadoes during 1996–2004. Preprints, *22nd Conf. on Severe Local Storms*, Hyannis, MA, Amer. Meteor. Soc., 15.4.
- , J. M. Straka, and E. N. Rasmussen, 1996a: Fine-scale Doppler radar observations of tornadoes. *Science*, **272**, 1774–1777.
- , —, and —, 1996b: Preliminary radar observations of the structure of tornadoes, Preprints, *18th Conf. on Severe Local Storms*, San Francisco, CA, Amer. Meteor. Soc., 17–22.
- , —, —, M. Randall, and A. Zahrai, 1997: Design and deployment of a portable, pencil-beam, pulsed 3-cm Doppler radar. *J. Atmos. Oceanic Technol.*, **14**, 1502–1512.
- , Y. Richardson, C. Alexander, S. Weygandt, and P. F. Zhang, 2007a: Dual-Doppler and single-Doppler analysis of a tornadic storm undergoing mergers and repeated tornadogenesis. *Mon. Wea. Rev.*, **135**, 736–758.
- , —, —, —, and —, 2007b: Dual-Doppler analysis of winds and vorticity budget terms near a tornado. *Mon. Wea. Rev.*, **135**, 2392–2405.
- , P. Robinson, C. Alexander, and Y. Richardson, 2007c: Low-level winds in tornadoes and potential catastrophic tornado impacts in urban areas. *Bull. Amer. Meteor. Soc.*, **88**, 31–46.
- , —, —, and K. A. Kosiba, 2008: Rapid-Scan DOW 3D GBVTD and traditional analysis of tornadogenesis, Preprints, *24th Conf. on Severe Local Storms*, Savannah, GA, Amer. Meteor. Soc., P13.6.
- , H. Bluestein, D. Burgess, D. Dowell, P. Markowski, Y. Richardson, and L. Wicker, 2010: VORTEX2: The Verification of the Origins of Rotation in Tornadoes Experiment. *Proc. Sixth European Conf. on Radar Meteorology and Hydrology*, Sibiu, Romania, European Meteorological Society, 10 pp. [Available online at http://www.erad2010.org/pdf/oral/wednesday/mesoscale/02_ERAD2010_0160.pdf.]
- Zehnder, J. A., J. Hu, and A. Razdan, 2007: A stereo photogrammetric technique applied to orographic convection. *Mon. Wea. Rev.*, **135**, 2265–2277.